Differential Cross Sections for Proton-Proton Elastic Scattering

Ryan B. Norman
University of Tennessee, Knoxville, Tennessee

Frank Dick
Worcester Polytechnic Institute, Worcester, Massachusetts

John W. Norbury and Steve R. Blattnig
Langley Research Center, Hampton, Virginia

NASA STI Program . . . in Profile

Since its founding, NASA has been dedicated to the advancement of aeronautics and space science. The NASA scientific and technical information (STI) program plays a key part in helping NASA maintain this important role.

The NASA STI program operates under the auspices of the Agency Chief Information Officer. It collects, organizes, provides for archiving, and disseminates NASA's STI. The NASA STI program provides access to the NASA Aeronautics and Space Database and its public interface, the NASA Technical Report Server, thus providing one of the largest collections of aeronautical and space science STI in the world. Results are published in both non-NASA channels and by NASA in the NASA STI Report Series, which includes the following report types:

- TECHNICAL PUBLICATION. Reports of completed research or a major significant phase of research that present the results of NASA programs and include extensive data or theoretical analysis. Includes compilations of significant scientific and technical data and information deemed to be of continuing reference value. NASA counterpart of peer-reviewed formal professional papers, but having less stringent limitations on manuscript length and extent of graphic presentations.

- TECHNICAL MEMORANDUM. Scientific and technical findings that are preliminary or of specialized interest, e.g., quick release reports, working papers, and bibliographies that contain minimal annotation. Does not contain extensive analysis.

- CONTRACTOR REPORT. Scientific and technical findings by NASA-sponsored contractors and grantees.

- CONFERENCE PUBLICATION. Collected papers from scientific and technical conferences, symposia, seminars, or other meetings sponsored or co-sponsored by NASA.

- SPECIAL PUBLICATION. Scientific, technical, or historical information from NASA programs, projects, and missions, often concerned with subjects having substantial public interest.

- TECHNICAL TRANSLATION. English-language translations of foreign scientific and technical material pertinent to NASA's mission.

Specialized services also include creating custom thesauri, building customized databases, and organizing and publishing research results.

For more information about the NASA STI program, see the following:

- Access the NASA STI program home page at *http://www.sti.nasa.gov*

- E-mail your question via the Internet to help@sti.nasa.gov

- Fax your question to the NASA STI Help Desk at 443-757-5803

- Phone the NASA STI Help Desk at 443-757-5802

- Write to:
  NASA STI Help Desk
  NASA Center for AeroSpace Information
  7115 Standard Drive
  Hanover, MD 21076-1320

NASA/TP-2009-215565

Differential Cross Sections for Proton-Proton Elastic Scattering

Ryan B. Norman
University of Tennessee, Knoxville, Tennessee

Frank Dick
Worcester Polytechnic Institute, Worcester, Massachusetts

John W. Norbury and Steve R. Blattnig
Langley Research Center, Hampton, Virginia

February 2009

Acknowledgments

Available from:

NASA Center for AeroSpace Information
7115 Standard Drive
Hanover, MD 21076-1320
443-757-5802

Contents

List of Figures

List of Tables

Nomenclature

Note: Units are used in which $c = \hbar = 1$.

c	speed of light
$\hbar$	Planck constant divided by 2π
l, lab	refers to lab frame
c, cm	refers to center of momentum frame
λ_{ij}	flux factor for masses i and j
E_i	energy of particle i
$\mathbf{p}_i$	3-momentum of particle i
p_i	4-momentum of particle i
q_j	4-momentum of internal particle j
$\mathcal{M}$	invariant amplitude
g	coupling constant
m_j	mass of particle j
m_π	mass of the pion
m_p	mass of the proton
$\mathcal{S}$	statistical factor
σ	total cross section
σ_d	total cross section due to direct term
σ_e	total cross section due to exchange term
σ_i	total cross section due to interference term
$d\sigma/dt$	invariant distribution (or differential cross section)
s, t, u	Mandelstam variables
t_0	value of variable t at $\theta = 0$
t_π	value of variable t at $\theta = \pi$
u_0	value of variable u at $\theta = 0$
u_π	value of variable u at $\theta = \pi$
s_t	$= s_{threshold}$, value of variable s at the reaction threshold
GeV	mass and energy unit, one billion electron volts
mb	millibarns
pb	picobarns
μb	microbarns

Abstract

Proton-proton elastic scattering is investigated within the framework of the one pion exchange model in an attempt to model nucleon-nucleon interactions spanning the large range of energies important to cosmic ray shielding. A quantum field theoretic calculation is used to compute both differential and total cross sections. A scalar theory is then presented and compared to the one pion exchange model. The theoretical cross sections are compared to proton-proton scattering data to determine the validity of the models.

1   Introduction

An accurate understanding of the elementary particle interactions in the energy range of the galactic cosmic ray (GCR) spectrum is important for the shielding of sensitive equipment and personnel on long duration space missions [1]. The cosmic ray spectrum ranges from approximately 100 MeV (10^6 eV) to 1 ZeV (10^{21} eV) with the region from 100 MeV to 10 GeV containing the bulk of the flux [2, 3]. While there are many models of the nuclear interactions that work well in a specific energy range, there is no single theory that gives calculable cross sections for the 100 MeV to 10 GeV energy region of high flux, let alone the complete cosmic ray spectrum. In order to determine the validity of current models of the strong force at energies of importance to the shielding of galactic cosmic rays, the one pion exchange model (OPEM) is investigated in this work. The OPEM has been shown to work well as a description of the nucleon-nucleon interaction in the energy region of 1-10 GeV [4]. In the OPEM, the interaction of nucleons is mediated by the exchange of a pion. The pion couples to the nucleons via a pseudoscalar interaction, and the invariant amplitude is calculated in a full field theoretic framework which includes spin and isospin.

Recently, the NASA heavy ion transport code, HZETRN, was extended to include the effects of pion and muon production in the meson and muon transport code MESTRN [1]. An important production mechanism of pions in the energy range of .5 to 3 GeV is through an intermediate resonance state. This region of energy is of significance to space radiation shielding because the galactic cosmic ray flux peaks there. The Δ-resonance has been shown [5] to account for the majority of the pion production cross section near 1 GeV. Currently, MESTRN does not include the production of particles from an intermediate resonant state.

MESTRN uses parameterizations of the inclusive cross section, $p + p \rightarrow \pi^\pm + X$ (where X is everything else allowed in the reaction), using high energy data for the direct production of pions from proton-proton interactions. In fact, due to the scarcity of total cross section (σ) data for this inclusive process, Lorentz invariant differential cross section ($E\frac{d^3\sigma}{dp^3}$) parameterizations were numerically integrated to get spectral cross section ($\frac{d\sigma}{dE}$) points [6]. These numerically integrated points were then used as "data" to fit parameterizations of the spectral cross section for pion production from proton-proton collisions. The preciseness of the spectral cross section parameterizations is limited by both the accuracy of the original parameterization of the Lorentz invariant differential cross section and the accuracy of the spectral cross section parameterization of the numerically integrated Lorentz invariant differential cross section parameterization. The

numerically integrated parameterizations were compared to total cross section data by Blattnig et al. in reference [6]. These data were very limited for the charged pions, consisting of only 3 data points in the laboratory kinetic energy range of approximately 10-25 GeV. From the perspective of radiation transport, this is not as desirable as one might hope, since the GCR spectrum peaks around 1 GeV/nucleon and drops by about an order of magnitude near 10 GeV/nucleon [2]. Since all of these issues stem from the parameterizations used, it would be useful to have the cross sections used in MESTRN developed from the physics of the interaction, not simply parameterizations. The addition of cross sections based on physical models and the inclusion of intermediate resonance states into MESTRN is the ultimate goal of this research.

A promising theoretical mechanism for including the Δ-resonance is through the one boson exchange model (OBEM) [7]. The OBEM is an extension of the OPEM that uses the exchange of virtual mesons in addition to the pion to mediate the strong force at low energies where perturbative quantum chromodynamics (QCD) is unfeasible. As a first step in the implementation of this model into the physics of MESTRN, proton-proton elastic scattering is considered using the framework of the OPEM. In general, however, nucleon-nucleon elastic scattering is important to transport codes that include trapped radiation and solar radiation environments. The theoretical cross sections of the OPEM, both total and differential, are then compared to experimental data.

Deterministic transport codes require simple formulas for both total and differential cross sections in order to minimize the computational power required for shielding analysis. With that in mind, the simplest possible theories should be used whenever possible and therefore a scalar theory is presented in addition to the OPEM. The scalar theory is based on the theory presented by Griffiths [8] and Kraus [9], called ABC theory. It is presented as a full quantum field theory and is compared to both the OPEM and experimental data in an attempt to give insight into the importance of spin at these energies.

2 Pseudoscalar Theory: One Pion Exchange Model

In the one pion exchange model, a virtual pion is used to mediate the force between two interacting nucleons. As the lightest meson, the pion has the longest interaction range and therefore is the dominant mechanism at low energies. As the incident nucleon's energy increases, the interaction range decreases, and the theoretical cross sections fit to the data should worsen. The inclusion of heavier bosons and multiple boson processes to the exchange mechanism has been shown to fit the data well at higher energies [10].

The Feynman rules for the OPEM with pseudoscalar coupling of the pion to the nucleon are presented below and the Feynman diagrams are shown in Figure 1.

1. Interaction Lagrangian:

$$\mathcal{L}_{\pi NN} = -ig_{\pi NN}\bar{\Psi}\gamma_5\boldsymbol{\tau}\cdot\boldsymbol{\pi}\Psi. \tag{1}$$

2. Vertex:

$$-ig_{\pi NN}\gamma_5\tau_i. \tag{2}$$

3. Propagator:

$$\frac{i\delta_{ij}}{q^2 - m_\pi^2}.$$

(3)

In the above, Ψ is the nucleon field and $\boldsymbol{\pi}$ is the pion field. $\boldsymbol{\tau}$ are the usual Pauli isospin matrices. γ_5 is the product of Dirac gamma matrices and is equal to $-i\gamma_0\gamma_1\gamma_2\gamma_3$. $g_{\pi NN}$ is the coupling constant of the pion-nucleon-nucleon vertex and q is the momentum of the exchange particle, the pion. In Equation 1, one can expand the fields as $\bar{\Psi}\boldsymbol{\tau} \cdot \boldsymbol{\pi}\Psi = \sqrt{2}\bar{p}n\pi^- + \sqrt{2}\bar{n}p\pi^+ + \bar{p}p\pi^0 - \bar{n}n\pi^0$ (see Appendix A).

2.1 Invariant Amplitude

For proton-proton (pp) elastic scattering, the t channel (direct channel) amplitude is given by Feynman's rules corresponding to Figure 1(a),

$$i\mathcal{M}_d = \frac{i\delta_{ij}g_{\pi NN}}{t - m_\pi^2}(\bar{\Psi}_3\tau_i\gamma_5\Psi_1)(\bar{\Psi}_4\tau_j\gamma_5\Psi_2).$$

(4)

The u channel (exchange channel) amplitude for pp elastic scattering, corresponding to Figure 1(b), is given as

$$i\mathcal{M}_e = \frac{i\delta_{ij}g_{\pi NN}}{u - m_\pi^2}(\bar{\Psi}_4\tau_i\gamma_5\Psi_1)(\bar{\Psi}_3\tau_j\gamma_5\Psi_2),$$

(5)

where $\Psi_i = \Psi(p_i)$. t and u are defined as

$$t \equiv (p_1 - p_3)^2,$$

(6)

$$u \equiv (p_1 - p_4)^2,$$

(7)

and p_i is the 4-momentum of the ith particle.

Now, isolate the isospin terms in the invariant amplitudes and group them together in the following way,

$$\delta_{ij}\tau_i\tau_j = \tau_i\tau_i \equiv I.$$

(8)

It should be noted that the isospin factors, I, must be the same for both the direct and exchange channels since this is proton-proton elastic scattering. For clarity, the terms I_d and I_e, corresponding to the direct and exchange terms, will remain in the calculation until the very end.

To compute the cross section, square the total invariant amplitude and sum over the final spin states and average over the initial spin states.

$$\frac{1}{4}\sum_{spins}|\mathcal{M}|^2 = \frac{1}{4}\sum_{spins}(|\mathcal{M}_d|^2 + |\mathcal{M}_e|^2 - \mathcal{M}_d^*\mathcal{M}_e - \mathcal{M}_e^*\mathcal{M}_d).$$

(9)

3
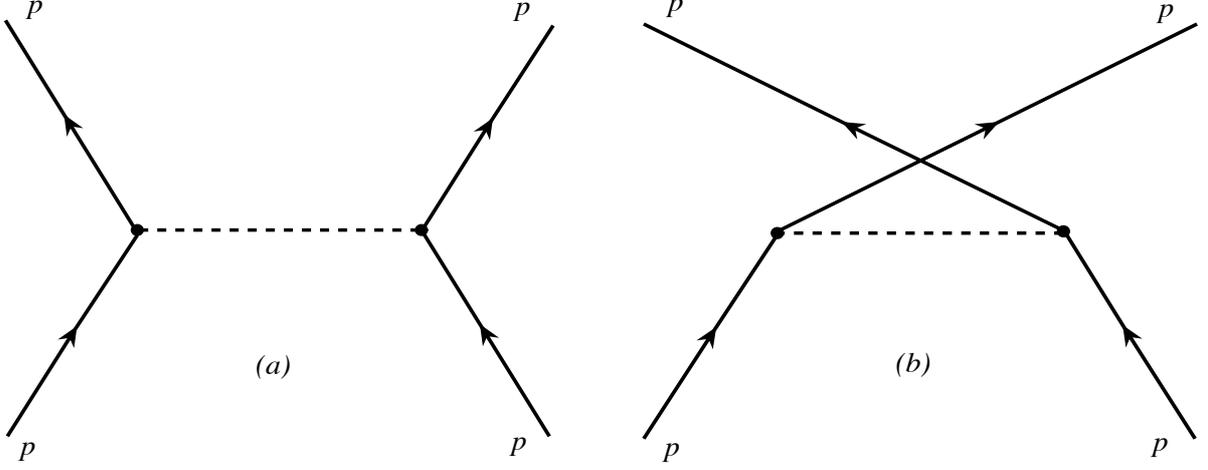
Figure 1: The Feynman diagrams of the direct and exchange amplitudes that contribute to the proton-proton elastic scattering process.

Now, look at each term in Equation 9 separately.

$$\frac{1}{4}\sum_{spins}|\mathcal{M}_d|^2 = \sum_{spins}\frac{g_{\pi NN}^4 I_d^2}{4(t-m_\pi^2)^2}(\bar{\Psi}_4\gamma_5\Psi_1)(\bar{\Psi}_4\gamma_5\Psi_1)^*(\bar{\Psi}_3\gamma_5\Psi_2)(\bar{\Psi}_3\gamma_5\Psi_2)^*. \tag{10}$$

Use the following to simplify Equation 10.

$$(\bar{\Psi}_i\gamma_5\Psi_j)^* = \Psi_j^\dagger\gamma_5^\dagger\gamma_0^\dagger\Psi_i = \Psi_j^\dagger\gamma_5\gamma_0\Psi_i = -\Psi_j^\dagger\gamma_0\gamma_5\Psi_i = -\bar{\Psi}_j\gamma_5\Psi_i. \tag{11}$$

Using this, one obtains

$$\frac{1}{4}\sum_{spins}|\mathcal{M}_d|^2 = \sum_{spins}\frac{g_{\pi NN}^4 I_d^2}{4(t-m_\pi^2)^2}(\bar{\Psi}_4\gamma_5\Psi_1)(\bar{\Psi}_1\gamma_5\Psi_4)(\bar{\Psi}_3\gamma_5\Psi_2)(\bar{\Psi}_2\gamma_5\Psi_3). \tag{12}$$

The sum over the spins is performed using the convention of Peskin and Schroeder [11] where

$$\sum_s \Psi^s\bar{\Psi}^s = \not{p}+m, \tag{13}$$

$$\frac{1}{4}\sum_{spins}|\mathcal{M}_d|^2 = \frac{g_{\pi NN}^4 I_d^2}{4(t-m_\pi^2)^2}Tr[(\not{p}_4+m_p)\gamma_5(\not{p}_1+m_p)\gamma_5]$$
$$\times Tr[(\not{p}_3+m_p)\gamma_5(\not{p}_2+m_p)\gamma_5], \tag{14}$$

where $\not{p}_i = \gamma_\mu p_i^\mu$ and

$$Tr(\text{odd number of gammas}) = 0, \tag{15}$$

$$\gamma_5\gamma_5 = \begin{pmatrix} 1 & 0 & 0 & 0 \\ 0 & 1 & 0 & 0 \\ 0 & 0 & 1 & 0 \\ 0 & 0 & 0 & 1 \end{pmatrix}. \tag{16}$$

4

Using the above, evaluate the traces to obtain the direct contribution to the invariant amplitude,

$$\frac{1}{4}\sum_{spins}|\mathcal{M}_d|^2 = \frac{g_{\pi NN}^4 I_d^2}{4(t-m_\pi^2)^2}(-4p_3 \cdot p_1 + 4m_p^2)(-4p_4 \cdot p_2 + 4m_p^2). \tag{17}$$

From Equations 6 and 7, one can see that

$$\begin{aligned} t &= (p_1-p_3)^2 \\ &= p_1^2 + p_3^2 - 2p_1 \cdot p_3 \\ &= 2m_p^2 - 2p_1 \cdot p_3, \end{aligned} \tag{18}$$

$$\Longrightarrow p_1 \cdot p_3 = m_p^2 - \frac{1}{2}t, \tag{19}$$

but $t = (p_2 - p_4)^2$ also. This implies that

$$p_2 \cdot p_4 = p_1 \cdot p_3 = m_p^2 - \frac{1}{2}t. \tag{20}$$

Examination of the Mandelstam variables u and s yields

$$\begin{aligned} u &= (p_1-p_4)^2 \\ &= (p_2-p_3)^2, \end{aligned} \tag{21}$$

$$\Longrightarrow p_1 \cdot p_4 = m_p^2 - \frac{1}{2}u$$

$$p_2 \cdot p_3 = m_p^2 - \frac{1}{2}u, \tag{22}$$

$$\begin{aligned} s &= (p_1+p_2)^2 \\ &= (p_3+p_4)^2, \end{aligned} \tag{23}$$

$$\Longrightarrow p_1 \cdot p_2 = \frac{1}{2}s - m_p^2$$

$$p_3 \cdot p_4 = \frac{1}{2}s - m_p^2. \tag{24}$$

Returning to Equation 10, one can make some simplifications.

$$\begin{aligned} \frac{1}{4}\sum_{spins}|\mathcal{M}_d|^2 &= \frac{g_{\pi NN}^4 I_d^2}{4(t-m_\pi^2)^2}(-4p_3 \cdot p_1 + 4m_p^2)(-4p_4 \cdot p_2 + 4m_p^2) \\ &= \frac{g_{\pi NN}^4 I_d^2}{4(t-m_\pi^2)^2}(-4(m_p^2 - \frac{1}{2}t) + 4m_p^2)(-4(m_p^2 - \frac{1}{2}t) + 4m_p^2) \\ &= \frac{g_{\pi NN}^4 I_d^2 t^2}{(t-m_\pi^2)^2}. \end{aligned} \tag{25}$$

To calculate the second term in Equation 10, replace $t \to u$ in Equation 25. Therefore,

$$\frac{1}{4} \sum_{spins} |\mathcal{M}_e|^2 = \frac{g_{\pi NN}^4 I_e^2 u^2}{(u - m_\pi^2)^2}. \tag{26}$$

Upon calculating the first cross term, one finds

$$
\begin{aligned}
\frac{1}{4} \sum_{spins} \mathcal{M}_d^* \mathcal{M}_e &= \sum_{spins} \frac{g_{\pi NN}^4 I_d^* I_e}{4(t - m_\pi^2)(u - m_\pi^2)} (\bar{\Psi}_4 \gamma_5 \Psi_1)(\bar{\Psi}_3 \gamma_5 \Psi_2) \\
&\quad \times (\bar{\Psi}_2 \gamma_5 \Psi_4)(\bar{\Psi}_1 \gamma_5 \Psi_3) \\
&= \frac{g_{\pi NN}^4 I_d^* I_e}{4(t - m_\pi^2)(u - m_\pi^2)} Tr[(\not{p}_4 + m_p)\gamma_5(\not{p}_1 + m_p) \\
&\quad \times \gamma_5(\not{p}_3 + m_p)\gamma_5(\not{p}_2 + m_p)\gamma_5] \\
&= \frac{g_{\pi NN}^4 I_d^* I_e}{4(t - m_\pi^2)(u - m_\pi^2)} [(\frac{1}{2}u - m_p^2)^2 - (\frac{1}{2}s - m_p^2)^2 \\
&\quad + (\frac{1}{2}t - m_p^2)^2 - 4m_p^4].
\end{aligned} \tag{27}
$$

Looking at the other cross term,

$$
\begin{aligned}
\frac{1}{4} \sum_{spins} \mathcal{M}_e^* \mathcal{M}_d &= \sum_{spins} \frac{g_{\pi NN}^4 I_d I_e^*}{4(t - m_\pi^2)(u - m_\pi^2)} (\bar{\Psi}_2 \gamma_5 \Psi_3)(\bar{\Psi}_1 \gamma_5 \Psi_4) \\
&\quad \times (\bar{\Psi}_3 \gamma_5 \Psi_1)(\bar{\Psi}_4 \gamma_5 \Psi_2) \\
&= \frac{g_{\pi NN}^4 I_d I_e^*}{4(t - m_\pi^2)(u - m_\pi^2)} Tr[(\not{p}_2 + m_p)\gamma_5(\not{p}_3 + m_p)\gamma_5 \\
&\quad \times \not{p}_1 + m_p)\gamma_5(\not{p}_4 + m_p)\gamma_5] \\
&= \frac{g_{\pi NN}^4 I_d^* I_e}{4(t - m_\pi^2)(u - m_\pi^2)} [(\frac{1}{2}u - m_p^2)^2 - (\frac{1}{2}s - m_p^2)^2 \\
&\quad + (\frac{1}{2}t - m_p^2)^2 - 4m_p^4].
\end{aligned} \tag{28}
$$

Also, note that in the case of elastic scattering, the isospin factors are both equal to unity ($I_d = I_e = 1$). Therefore, the total spin averaged and summed invariant amplitude is

$$
\begin{aligned}
\frac{1}{4} \sum_{spins} |\mathcal{M}|^2 &= g_{\pi NN}^4 \left\{ \frac{t^2}{(t - m_\pi^2)^2} + \frac{u^2}{(u - m_\pi^2)^2} - \frac{2}{4(t - m_\pi^2)(u - m_\pi^2)} \right. \\
&\quad \left. \times \left[(\frac{1}{2}u - m_p^2)^2 - (\frac{1}{2}s - m_p^2)^2 + (\frac{1}{2}t - m_p^2)^2 - 4m_p^4 \right] \right\}.
\end{aligned} \tag{29}
$$

6

2.2 Cross Section

Now that the invariant amplitude is calculated, the next step is to calculate the total cross section. The differential cross section is given as

$$\frac{d\sigma}{dt} = \frac{S}{16\pi\lambda_{12}} \frac{1}{4} \sum_{spin} |\mathcal{M}|^2, \tag{30}$$

where

$$\lambda_{ij} \equiv (s - m_i^2 - m_j^2)^2 - 4m_i^2 m_j^2, \tag{31}$$

$$\lambda_{12} = s(s - 4m_p^2), \tag{32}$$

$$s \equiv (p_1 + p_2)^2$$

$$= E_{cm}^2, \tag{33}$$

and the statistical factor S is given by $\frac{1}{j!}$ for j identical particles in the final state. In the case of elastic scattering of protons, $S = \frac{1}{2}$. The total cross section is then

$$\sigma = \int_{t_\pi}^{t_0} \frac{d\sigma}{dt} dt. \tag{34}$$

The limits of the integration (see Appendix B for a derivation) are given as

$$t_0(t_\pi) \equiv \frac{1}{4s} \left[(m_1^2 - m_2^2 - m_3^2 + m_4^2)^2 - (\sqrt{\lambda_{12}} \mp \sqrt{\lambda_{34}})^2 \right], \tag{35}$$

which yields

$$t_0 = 0, \tag{36}$$

$$t_\pi = 4m_p^2 - s. \tag{37}$$

To simplify the calculation, the total cross section is broken into parts: the direct, exchange, and interference parts,

$$\sigma = \sigma_d + \sigma_e + \sigma_i. \tag{38}$$

This method simplifies the integration. A new variable, K, is defined as,

$$K \equiv \frac{g_{\pi NN}^4 S}{16\pi\lambda_{12}}$$

$$= \frac{g_{\pi NN}^4}{32\pi s(s - 4m_p^2)}. \tag{39}$$

The direct channel cross section is

$$\sigma_d = K \int_{t_\pi}^{t_0} \frac{t^2}{(t - m_\pi^2)^2} dt$$

$$= K \left[\frac{(s - 4m_p^2)(4m_p^2 - 2m_\pi^2 - s)}{4m_p^2 - s - m_\pi^2} + 2m_\pi^2 ln\left(\frac{m_\pi^2}{s + m_\pi^2 - 4m_p^2} \right) \right]. \tag{40}$$

7

For the exchange channel, one notices that

$$
\begin{align}
u &= 4m_p^2 - s - t, \tag{41}\\
du &= -dt, \tag{42}\\
t_\pi &= u_0, \tag{43}\\
t_0 &= u_\pi. \tag{44}
\end{align}
$$

This implies that

$$
\begin{align}
\sigma_e &= K \int_{t_\pi}^{t_0} \frac{u^2}{(u - m_\pi^2)^2} dt \notag\\
&= K \int_{4m_p^2 - s}^{0} \frac{u^2}{(u - m_\pi^2)^2} du, \tag{45}\\
\implies \sigma_d &= \sigma_e. \tag{46}
\end{align}
$$

The interference cross section is

$$
\begin{align}
\sigma_i &= -\frac{K}{2} \int_{t_\pi}^{t_0} \frac{(\frac{1}{2}u - m_p^2)^2 - (\frac{1}{2}s - m_p^2)^2 + (\frac{1}{2}t - m_p^2)^2 - 4m_p^4}{(t - m_\pi^2)(u - m_\pi^2)} dt \notag\\
&= -\frac{K}{2} \int_{4m_p^2 - s}^{0} \frac{\frac{1}{2}t^2 + t(\frac{1}{2}s - 2m_p^2) - 3m_p^4}{(t - m_\pi^2)(4m_p^2 - s - t - m_\pi^2)} dt \notag\\
&= -\frac{K}{2} \left[2m_p^2 - \frac{1}{2}s + \frac{\frac{1}{8}(s + 2m_\pi^2)^2 - m_p^4 - m_p^2(s + 2m_\pi^2)}{s + 2m_\pi^2 - 4m_p^2} ln\left(\frac{s + m_\pi^2 - 4m_p^2}{m_\pi^2} \right) \right]. \tag{47}
\end{align}
$$

Therefore, the total cross section is

$$
\begin{align}
\sigma &= \sigma_d + \sigma_e + \sigma_i \notag\\
&= \frac{g_{\pi NN}^4}{16\pi s(s - 4m_p^2)} \left\{ \frac{(s - 4m_p^2)(4m_p^2 - 2m_\pi^2 - s)}{4m_p^2 - s - m_\pi^2} + 2m_\pi^2 ln\left(\frac{m_\pi^2}{s + m_\pi^2 - 4m_p^2} \right) \right. \notag\\
&\quad \left. -\frac{1}{4} \left[2m_p^2 - \frac{1}{2}s + \frac{\frac{1}{8}(s + 2m_\pi^2)^2 - m_p^4 - m_p^2(s + 2m_\pi^2)}{s + 2m_\pi^2 - 4m_p^2} ln\left(\frac{s + m_\pi^2 - 4m_p^2}{m_\pi^2} \right) \right] \right\}. \tag{48}
\end{align}
$$

3   Scalar Theory: Scalar One Pion Exchange Model

A simple scalar theory is presented in reference [8] (often called ABC theory) and provides a good check of whether spin is important to calculations of this kind. In this theory, only scalar fields couple to each other. The rules of this theory for elastic scattering are given below.

1. Interaction Lagrangian:

$$
\mathcal{L}_{scalar} = -igAAB. \tag{49}
$$

2. Vertex:

$$
-ig. \tag{50}
$$

3. Propagator:

$$\frac{i}{q^2 - m_\pi^2}.$$

(51)

In the above equations, A and B are scalar fields obeying the Klein-Gordon equation, g is the coupling constant, and once again, q is the exchange particle 4-momentum.

3.1 Invariant Amplitude

With this simple theory, one can immediately write down the total invariant amplitude.

$$\mathcal{M} = \frac{g^2}{t - m_\pi^2} + \frac{g^2}{u - m_\pi^2}.$$

(52)

To compute the total cross section, square the invariant amplitude $\mathcal{M}$.

$$|\mathcal{M}|^2 = \frac{g^4}{(t - m_\pi^2)^2} + \frac{g^4}{(u - m_\pi^2)^2} + \frac{2g^4}{(t - m_\pi^2)(u - m_\pi^2)}.$$

(53)

3.2 Cross Section

To calculate the total cross section, we follow the method used for the pseudoscalar theory and consider the terms of Equation 53 separately in evaluating the total cross section. Similar to Equation 30,

$$\frac{d\sigma}{dt} = \frac{S}{16\pi\lambda_{12}}|\mathcal{M}|^2,$$

(54)

with λ_{12} being defined in Equation 32.

The total cross section is given by Equation 34 with the limits specified by Equation 35. Once again, the statistical factor $S = \frac{1}{2}$. Again, define a variable N to make our equations simpler.

$$
\begin{aligned}
N &= \frac{g^4 S}{16\pi\lambda_{12}} \\
&= \frac{g^4}{32\pi s(s - 4m_p^2)}.
\end{aligned}
$$

(55)

The direct channel cross section (the contribution from the first term in Equation 53) is

$$
\begin{aligned}
\sigma_d &= N \int_{t_\pi}^{t_0} \frac{1}{(t - m_\pi^2)^2} dt \\
&= \left. \frac{N}{m_\pi^2 - t} \right|_{4m_p^2 - s}^{0} \\
&= N\left(\frac{1}{m_\pi^2} - \frac{1}{s + m_\pi^2 - 4m_p^2} \right).
\end{aligned}
$$

(56)

9

Once again, it is shown that $\sigma_d = \sigma_e$. Recall that

$$u = 4m_p^2 - s - t, \tag{57}$$

$$du = -dt, \tag{58}$$

$$t_\pi = u_0, \tag{59}$$

$$t_0 = u_\pi. \tag{60}$$

It can once again be shown that

$$\sigma_e = N \int_{t_\pi}^{t_0} \frac{1}{(u - m_\pi^2)^2} dt$$

$$= N \int_{4m_p^2 - s}^{0} \frac{1}{(u - m_\pi^2)^2} du, \tag{61}$$

$$\implies \sigma_d = \sigma_e. \tag{62}$$

All that remains is to calculate the interference term.

$$\sigma_i = 2N \int_{t_\pi}^{t_0} \frac{1}{(t - m_\pi^2)(u - m_\pi^2)} dt$$

$$= 2N \int_{4m_p^2 - s}^{0} \frac{1}{(t - m_\pi^2)(4m_p^2 - s - t - m_\pi^2)} dt$$

$$= \frac{2N}{s + 2m_\pi^2 - 4m_p^2} ln\left(\frac{t + s + m_\pi^2 - 4m_p^2}{t - m_\pi^2}\right)\Big|_{4m_p^2 - s}^{0}$$

$$= \frac{4N}{s + 2m_\pi^2 - 4m_p^2} ln\left(\frac{s + m_\pi^2 - 4m_p^2}{m_\pi^2}\right). \tag{63}$$

Therefore, the total cross section is

$$\sigma = \sigma_d + \sigma_e + \sigma_i \tag{64}$$

$$= 2N\left[\frac{1}{m_\pi^2} - \frac{1}{s + m_\pi^2 - 4m_p^2}\right.$$

$$\left. + \frac{2}{s + 2m_\pi^2 - 4m_p^2} ln\left(\frac{s + m_\pi^2 - 4m_p^2}{m_\pi^2}\right)\right]$$

$$= \frac{g^4}{16\pi s(s - 4m_p^2)}\left[\frac{1}{m_\pi^2} - \frac{1}{s + m_\pi^2 - 4m_p^2}\right.$$

$$\left. + \frac{2}{s + 2m_\pi^2 - 4m_p^2} ln\left(\frac{s + m_\pi^2 - 4m_p^2}{m_\pi^2}\right)\right]. \tag{65}$$

10

4 Total Cross Section in the Asymptotic Region

Now that the total cross sections for both the scalar theory (Equation 65) and the OPEM (Equation 48) have been calculated, the theoretical cross sections are investigated to make sure that they do not have any odd behavior that may cause problems when the cross sections are used in computer codes such as MESTRN. The first thing to examine is the limit of the cross section as s approaches its threshold value of $4m_p^2$. The scalar theory gives

$$\lim_{s \to 4m_p^2} \sigma_{scalar} = \frac{3g^4}{64\pi m_p^2 m_\pi^4}. \tag{66}$$

The OPEM gives:

$$\lim_{s \to 4m_p^2} \sigma_{OPEM} = \frac{g^4(m_\pi^4 + 6m_p^4)}{1024 m_p^2 m_\pi^4}. \tag{67}$$

From both a physical understanding viewpoint and an applications perspective, the cross section must be well behaved in order to have physical meaning and application. In this case, both models are finite at threshold energy.

The cross sections should also obey the Froissart bound [12] which states that

$$\lim_{s \to \infty} \sigma_{total} < c(log\ s)^2, \tag{68}$$

where c is a constant and σ_{total} is the elastic plus inelastic cross section.

Next, compute the limits of the cross sections as $s \to \infty$. The scalar theory gives

$$\lim_{s \to \infty} \sigma_{scalar} = 0, \tag{69}$$

and the OPEM model gives

$$\lim_{s \to \infty} \sigma_{OPEM} = 0. \tag{70}$$

While the Froissart bound applies to the inelastic plus the elastic cross section, it is still a good test of the physical validity of our theories. Both the OPEM and the scalar model elastic cross sections obey the Froissart bound (see Figure 2).

The result that, in the limit of large s, the theoretical cross sections go to zero is not surprising. As the energy increases, the likelihood of an inelastic reaction occurring increases as more inelastic channels become available. This decreases the possible phase space available to the elastic channel, thus decreasing the likelihood of an elastic interaction.

5 Comparison of the Models

Now that the models have been developed, they must be compared to experimental data (see Appendix D) to determine their usefulness. To do this, the coupling constant is left as a free parameter and used to fit the value of the theoretical curve to the experimental data at one

11

point. When the scalar theory is compared to the pseudoscalar theory, over all energy ranges and for the majority of the data sets, the scalar theory is the better fit (see Figures 3–40). This is especially true for the invariant differential cross sections in the region of t close to zero, as will be discussed below. In general, the pseudoscalar pion exchange of the OPEM tends to severely underestimate the invariant differential cross section in this region. While the scalar theory fits the data well in this region, as t approaches 0 it tends to overestimate the data (see below).

As another test of how well these theories fit the data, a simple parameterization [13] is also introduced. For the total cross section, the Bertsch parameterization (units of mb) gives:

$$
\begin{aligned}
\sigma(\sqrt{s}) &= 55 && \text{if } \sqrt{s} < 1.8993 \,\text{GeV} \\
&= \frac{35}{1 + 200(s - 1.8993)} + 20 && \text{if } \sqrt{s} > 1.8993 \,\text{GeV},
\end{aligned} \tag{71}
$$

and for the invariant differential cross section, it gives

$$
\frac{d\sigma}{dt} = ae^{bt}, \tag{72}
$$

where b is defined as

$$
b(\sqrt{s}) = \frac{6(3.65(\sqrt{s} - 1.866))^6}{1 + (3.65(\sqrt{s} - 1.866))^6}, \tag{73}
$$

and the variable a is taken as a parameter that is used to fit to the data.

5.1   Total Cross Section

An overall view of the total cross section curves, along with experimental data from the Particle Data Group [14] in the momentum range of 0 to 10 GeV is shown in Figure 3. Figure 3 shows the OPEM and the scalar model providing a good fit to the data in the low energy region. As will be discussed in the next section, the scalar theory does an excellent job of fitting the data in this region. As the momentum increases, the OPEM and the scalar theory fall off too quickly to represent the experimental data when using a coupling constant appropriate for low momentum. A discussion of this is presented below.

Figure 4 shows that the scalar and pseudoscalar pion exchange models fit the data well below approximately .5 GeV. The scalar theory does slightly better compared to the OPEM for this momentum range. When the incident lab momentum, p_{lab}, becomes greater than .5 GeV the theoretical curves fall off very quickly compared to the data. In the .5 GeV to 1 GeV momentum range, both models begin to slightly underestimate the data. The parameterization of Bertsch [13] (labeled as Bertsch on the graphs) works well for 1 GeV $> p_{lab} > $ .5 GeV but is definitely not appropriate below .5 GeV since it has a discontinuity at $p_{lab} = .3003$ GeV and underestimates the cross section in this region significantly. This can be seen in Figure 4.

As the incident particle momentum in the lab frame increases, the theoretical curves for both the OPEM and scalar model are shown to be poor representations of the data (see Figure 5). This is partially due to the decaying functional form of the model cross sections. In the lab momentum range of 1 to 2, GeV the Bertsch parameterization works well.

As the lab momentum is increased further, the Bertsch parameterization begins to overestimate the data. This behavior begins in the 2 to 5 GeV region (see Figure 6). It is at this point that the relative error of the Bertsch parameterization begins to increase steadily to approximately 100% for the entire momentum range of 5 GeV to 50 GeV, while the OPEM and scalar model both underestimate the data (see Figure 7). This signals the failure of the models and indicates the need for a more complex theory to account for the larger cross section in this momentum range. The failure of the models at high energies is not a suprise. Any theory based solely on the exchange of a pion should begin to fail at higher energies as heavier exchange particles become more important.

5.1.1 The Coupling Constants

As was shown in Figure 3, the coupling constant used to fit the experimental data in the very low momentum region does not fit the experimental data at higher momentum. Using the momentum ranges of 1–2 GeV, 2–10 GeV and 10–50 GeV, the coupling constant for both the OPEM and the scalar model were varied to determine if the data could be broken up into momentum regions and ascertain whether different coupling constants could be used to reproduce the data in these regions. This is shown in Figures 5–7. In general, it was found that increasing the coupling constant of either theory led to the exaggeration of the curvature of the theoretical cross section. This is due to the coupling constant being a multiplicative parameter in the cross section formulas. Increasing the coupling constant inherently shifts the curves up slightly, but due to the quick decay of the cross section, simply changing the coupling constant is not enough to produce exact fits to the data.

In Figure 5, the data seem to be approximately constant over the momentum range. The models, however, have decreasing slope. The increased coupling constant fits the data much better than the one used in the very low momentum region for both theories, but does not have the correct slope.

Figure 6 shows that the OPEM fits the data very well with a coupling constant value of 11.5. The scalar theory does fairly well also, but the curve falls off faster than the OPEM.

In the 10 to 50 GeV range (Figure 7), the experimental cross section becomes constant again and both theories fall off too quickly with increasing momentum to fit the data precisely.

5.2 Invariant Differential Cross Section

In Figures 8–40, the invariant differential cross section ($\frac{d\sigma}{dt}$) data collected by various experiments is presented and compared to the models and the parameterization. For each momentum value, a unique coupling constant was fit to the data for each of the different theories and for the Bertsch parameterization. It is important to note that the coupling constant for the scalar theory has dimensions of energy, while the coupling constant of the OPEM is dimensionless, and an analysis of the coupling constants was not performed.

5.2.1 Data from Albrow et al., 1970

For Figures 8–10, data were taken from Albrow et al. [15] at 3 different momenta. At $p_{lab} = 1.118$ GeV (Figure 8), the theoretical curves, especially the OPEM theory, work quite well. The

OPEM fits the data at this momentum well with only a few percent error for the majority of the data points. As the incident lab momentum is increased to 1.38 GeV (Figure 9), the scalar theory becomes a slightly better fit than the OPEM, while the Bertsch parameterization is a relatively poor fit. At $p_{lab} = 2.74$ GeV (Figure 10), the fit to the data is better for the Bertsch parameterization than the theoretical curves.

5.2.2   Data from Dobrovolsky et al., 1988

For the data taken from Dobrovolsky et al. [16], which are all at low momentum (1.39 GeV to 1.68 GeV) and correspond to values of t very close to zero, the Bertsch parameterization is the best fit to the data. This is shown in Figures 11–14. The slopes of the two theoretical curves are too steep to fit the data well in these regions.

5.2.3   Data from Jenkins et al., 1980

In Figures 15–22, the data of Jenkins et al. [17] with a momentum range of 1.896 GeV to 8.022 GeV are compared with the 3 curves. One thing to note is that as t approaches zero, the differential cross section should increase [17] and therefore the data points that fall off as t approaches zero should be disregarded. With this in mind, over the whole momentum range the scalar theory is the closest fit. The slope of the Bertsch parameterization is too steep to fit the data well over the whole range of t. The OPEM does fit the data well in the region further away from zero. The scalar theory does a very good job of fitting the data. The only area where it seems to have some problems is at the lowest momentum, where it tends to underestimate the cross section data.

5.2.4   Data from Ambats et al., 1974

In Figures 23–26, the data were taken from Ambats et al. [18] and is in the momentum range of 3.00 GeV to 6.00 GeV. These data were taken over a wide range of t values. As t approaches zero, for all values of momentum in these data sets, the curves fall away from the data fairly significantly. At approximately $t > -.5$ GeV^2, the OPEM begins to increasingly underestimate the data. As t continues to get closer to zero, the scalar theory starts to overestimate the cross section while the parameterization of Bertsch tends to underestimate it. This trend is true across the entire data set. Notice that at values of t away from zero, the scalar theory does a very good job of fitting the data. This can especially be seen in Figures 24–26.

5.2.5   Data from Baglin et al., 1975

At a lab momentum of 9 GeV, the data of Baglin et al. [19] are used in Figure 27. The theoretical curves of the scalar theory and OPEM both fail when fit to this data set. As has been seen in previous data sets, the OPEM does not start rising in value until too close to zero to be able to fit the data well. In the case of the scalar theory, it does not have a steep enough slope to fit the data well but still gives a good general trend for the data. The Bertsch parameterization does a good job in the steeply increasing section near $t = -1$ GeV^2 but underestimates the cross section in the region $t < -1$ GeV^2.

14

5.2.6 Data from Brandenburg et al., 1975

When the 3 curves are plotted against the data presented by Brandenburg et al. [20] (Figure 28), the data are fit well by both the scalar theory and the Bertsch parameterization. These experimental data were taken at $p_{lab} = 10.4$ GeV. The OPEM severely underestimates the data in the t range close to zero. Figure 28 is another instance of the scalar theory being a good fit to the differential cross section data except in the t range close to zero. Surprisingly, the scalar theory fits the data fairly well in the t range far from zero.

5.2.7 Data from Beznogikh et al., 1973

The data gathered by Beznogikh et al. [21] are presented in Figures 29–35. These data spanned the momentum range of 9.43 GeV to 30.45 GeV. The t values for this data set were all very close to zero. All the curves follow the general trend of the data. For one set ($p_{lab} = 13.16$ GeV, Figure 30), the OPEM seems to do well, but overall the theoretical curves and the Bertsch parameterization are poor fits. Again, the tendency of the models to not fit the data well in the region of t close to zero is observed.

5.2.8 Data from Edelstein et al., 1972

In Figures 36 to 39, the data gathered by Edelstein et al. [22] were compared with the theoretical curves and the Bertsch parameterization. Those data were at higher momentum (9.9 GeV to 29.7 GeV) where the theoretical models are not thought to be valid. This data set spans a much larger t range than the Beznogikh data set and was used to determine how well the theoretical models are doing overall at higher momentum. Surprisingly, the scalar theory fits the data well up to $p_{lab} = 29.7$ GeV, as shown in Figure 39. The OPEM continues the general trend of doing well in the t range far from zero but severely underestimates the experimental cross section in the t region close to zero.

6 Conclusions

Two quantum field theoretic models of proton-proton elastic scattering were presented. One theoretical model, the one pion exchange model, contains full spin and isospin dependence, while the other theoretical model presented is based solely on scalar fields. The models were used to develop total and invariant differential cross sections that were then compared to data and a simple parameterization.

When the models were compared to the total cross section data available, it was found that the scalar theory was the best fit to the data below lab momentum of .5 GeV. This is an interesting result considering the simplicity of the scalar theory. Above a lab momentum of 3 GeV, both the theories and the Bertsch parameterization do poorly as fits to the total cross section data using the same coupling constant that was used in the very low momentum region. Increasing the coupling constant was found to give a better fit. The fit to the data, however, is not as good as was found in the very low momentum region.

For the invariant differential cross section data, the analysis is less straightforward. The data of seven papers were presented and the models were compared to these data, which included a laboratory momentum range of 1.38 GeV to 30.45 GeV. Over the complete data set that was investigated, the OPEM was the poorest fit. The scalar model and the Bertsch parameterization fit the data very well, until t approached zero (corresponding to the center of mass angle approaching zero). In the t close to zero range, the scalar theory tended to overestimate the data while the Bertsch parameterization underestimated. They both had a comparable error until the data came very close to zero, where the scalar theory tended to severely overestimate the data. The models began to fail when the laboratory momentum reached approximately 10 GeV.

With this analysis complete, the use of the OPEM by itself as the basis of the physics of proton-proton elastic scattering used in a radiation transport code (*i.e.* MESTRN) can be ruled out by the fact that in the regions in which it does work well, the scalar model does a better job of fitting the data. There is hope, however, that a more robust theory which includes heavier boson exchanges may make up for the failure of the OPEM. On the other hand, the scalar theory is the best model for total cross section in the momentum range below .5 GeV and can be used as a physical model of proton-proton elastic scattering.

For the case of the invariant differential cross section, the scalar model was the overall best fit to the data. The Bertsch parameterization has a major downfall in this case. Figure 40 shows the curves corresponding to the two theoretical models and the Bertsch parameterization plotted over the full physical region of t. The two theoretical models show the classic shape of two body differential cross sections (similar to Rutherford scattering), while the parameterization displays a simple exponential curve. This is disappointing considering the Bertsch parameterization is the best fit overall to all the data investigated in this paper. The scalar theory does a good job of fitting the data but overestimates in the t close to zero region. The scalar theory, however, was found to have the surprising result of fitting the differential data well at much higher incident momentum than would be expected of a simple scalar theory. The OPEM is a much poorer fit compared to the scalar theory as a general rule.

There is another subtlety associated with using the invariant differential cross sections of this paper in a transport code like MESTRN. The coupling constants were used as a free parameter to fit the data. The coupling constants were all found to vary with the laboratory momentum of the incident particle. The coupling constant for the OPEM varies from $g_{\pi NN} = 1.54$ to $g_{\pi NN} = 56.77$. While the coupling constant for the scalar theory varies from $g = 3.633$ GeV to $g = 25.10$ GeV and the coupling constant for the parameterization of Bertsch varies from $a = 24.14$ mb/GeV^2 to $a = 4.3 \times 10^9$ mb/GeV^2. This fitting procedure used in this paper allows the cross sections to be calculated only at the lowest order. The coupling constant then simulates the additional information contained in the higher order diagrams in the perturbation series. A detailed analysis would have to be performed to determine how the coupling constant should vary to achieve the best fit to the data over the entire physical momentum range.

In conclusion, the first step towards using cross sections based on physical interactions in NASA's radiation transport code MESTRN has begun with the investigation of proton-proton elastic scattering. It was found that a simple scalar model works very well in the low energy region when considering the total cross section and that more work needs to be done in the high

energy region to develop a physical model that fits the data well. The GCR spectrum ranges from about 100 MeV to 10 EeV (10^{19} eV), with the majority of the flux contained in the 100 MeV to 10 GeV region [2, 3]. There is no single theory that gives calculable cross sections for the 100 MeV to 10 GeV energy region of high flux, let alone the entire 14 orders of magnitude spanned by the complete cosmic ray spectrum.

Future work will include a detailed analysis of the coupling constants used in this paper and explore the effects of including higher order diagrams in the perturbation series. In addition, work needs to be done developing cross sections for other fundamental processes based on physical models, and the production of particles from intermediate resonance states must be investigated to obtain accurate cross sections, especially for pion production.

References

[1] S. R. Blattnig, J. W. Norbury, R. B. Norman, J. W. Wilson, R. C. Singleterry and R. K. Tripathi, NASA Technical Memorandum 212995 (2004).

[2] J. A. Simpson, Ann. Rev. Nucl. Part. Sci. **33**, 323 (1983).

[3] M. Durante, Riv. Nuovo Cimento **25**, 1 (2002).

[4] V. Dmitriev, O. Sushkov and C. Gaarde, Nucl. Phys. A **459**, 503 (1986).

[5] B. K. Jain and A. B. Santra, Phys. Rep. **230**, 1 (1993).

[6] S. R. Blattnig, S. R. Swaminathan, A. T. Kruger, M. Ngom and J. W. Norbury, Phys. Rev. D **62**, 094030 (2000).

[7] S. Huber and J. Aichelin, Nucl. Phys. A **573**, 587 (1994).

[8] D. Griffiths, *Introduction to Elementary Particles* (Wiley, New York, 1987).

[9] P. Kraus and D. J. Griffiths, Am. J. Phys. **60**, 1013 (1992).

[10] R. Machleidt, Adv. Nucl. Phys. **19**, 189 (1989).

[11] M. E. Peskin and D. V. Schroeder, *An Introduction to Quantum Field Theory* (Perseus Books, Reading, Massachusetts, 1995).

[12] M. Froissart, Phys. Rev. **123**, 1053 (1961).

[13] G. F. Bertsch and S. Das Gupta, Phys. Rep. **160**, 189 (1988).

[14] W.-M. Yao et al., J. Phys. G **33**, 1 (2006).

[15] M. G. Albrow, S. Andersson/Almehed, B. Bosnjakovic, C. Daum, F. C. Erne, J. P. Lagnaux, J. C. Sens and F. Udo, Nucl. Phys. B **23**, 445 (1970), The data were taken from the HEPDATA Reaction Database found at http://durpdg.dur.ac.uk/hepdata/reac.html.

[16] A. Dobrovolsky, A. Khanzadeev, G. Korolev, G. Velichko, A. Vorobev, J. Saudinos, B. Silverman, Y. Terrien and F. Wellers, Experimental data on elastic pp, np, pd and pγ forward scattering at intermediate-energies, LENINGRAD-88-1454, The data were taken from the HEPDATA Reaction Database found at http://durpdg.dur.ac.uk/hepdata/reac.html.

[17] K. A. Jenkins, L. E. Price, R. Klem, R. J. Miller, P. Schreiner, M. L. Marshak, E. A. Peterson and K. Ruddick, Phys. Rev. D **21**, 2445 (1980), The data were taken from the HEPDATA Reaction Database found at http://durpdg.dur.ac.uk/hepdata/reac.html.

[18] I. Ambats, D. S. Ayres, R. Diebold, A. F. Greene, S. L. Kramer, A. Lesnik, D. R. Rust, C. E. W. Ward, A. B. Wicklund and D. D. Yovanovitch, Phys. Rev. D **9**, 1179 (1974), The data were taken from the HEPDATA Reaction Database found at http://durpdg.dur.ac.uk/hepdata/reac.html.

[19] C. Baglin et al., Nucl. Phys. B **98**, 365 (1975), The data were taken from the HEPDATA Reaction Database found at http://durpdg.dur.ac.uk/hepdata/reac.html.

[20] G. Brandenburg, R. K. Carnegie, R. J. Cashmore, M. Davier, D. W. Leith, J. Matthews, P. Walden, S. H. Williams and F. Winkelmann, Phys. Lett. B **58**, 367 (1975), The data were taken from the HEPDATA Reaction Database found at http://durpdg.dur.ac.uk/hepdata/reac.html.

[21] G. G. Beznogikh et al., Nucl. Phys. B **54**, 78 (1973), The data were taken from the HEPDATA Reaction Database found at http://durpdg.dur.ac.uk/hepdata/reac.html.

[22] R. M. Edelstein et al., Phys. Rev. D **5**, 1073 (1972), The data were taken from the HEPDATA Reaction Database found at http://durpdg.dur.ac.uk/hepdata/reac.html.

Appendix A   Expansion of the OPEM interaction Lagrangian

This is a derivation of the expansion of the $\bar{\Psi}\boldsymbol{\tau}\cdot\boldsymbol{\pi}\Psi$ term that appears in the interaction Lagrangian of the OPEM (Eq. 1).

If we define the pion fields and the Pauli isospin matrices as

$$\pi^\pm = \frac{1}{\sqrt{2}}(\pi_1 \mp i\pi_2), \tag{74}$$

$$\pi^0 = \pi_3, \tag{75}$$

$$\tau^\pm = \frac{1}{\sqrt{2}}(\tau_1 \pm i\tau_2), \tag{76}$$

$$\tau^0 = \tau_3, \tag{77}$$

this implies that

$$\boldsymbol{\tau}\cdot\boldsymbol{\pi} = \tau_1\pi_1 + \tau_2\pi_2 + \tau_3\pi_3 \tag{78}$$

$$= \tau^+\pi^- + \tau^-\pi^+ + \tau^0\pi^0. \tag{79}$$

Using

$$\Psi = \begin{pmatrix} p \\ n \end{pmatrix}, \tag{80}$$

$$\bar{\Psi} = (\bar{p}\quad \bar{n}), \tag{81}$$

allows us to write

$$\mathcal{L}_{\pi NN} = -ig_{\pi NN}\bar{\Psi}\gamma_5\boldsymbol{\tau}\cdot\boldsymbol{\pi}\Psi \tag{82}$$

$$= -ig_{\pi NN}(\bar{p}\quad \bar{n})\gamma_5\Big[\sqrt{2}\begin{pmatrix} 0 & 1 \\ 0 & 0 \end{pmatrix}\pi^- + \sqrt{2}\begin{pmatrix} 0 & 0 \\ 1 & 0 \end{pmatrix}\pi^+$$

$$+ \begin{pmatrix} 1 & 0 \\ 0 & -1 \end{pmatrix}\pi^0\Big]\begin{pmatrix} p \\ n \end{pmatrix} \tag{83}$$

$$= -ig_{\pi NN}(\sqrt{2}\bar{p}\gamma_5 n\pi^- + \sqrt{2}\bar{n}\gamma_5 p\pi^+ + \bar{p}\gamma_5 p\pi^0 - \bar{n}\gamma_5 n\pi^0). \tag{84}$$

Appendix B   Derivation of t_0 and t_π

This is the derivation of the limits of integration for Equation 35. In any reference frame,

$$
\begin{aligned}
t &\equiv (p_1 - p_3)^2 \\
&= (E_1 - E_3)^2 - (\boldsymbol{p}_1 - \boldsymbol{p}_3)^2.
\end{aligned}
\tag{85}
$$

Now, look at only the momentum piece:

$$
\begin{aligned}
(\boldsymbol{p}_1 - \boldsymbol{p}_3)^2 &= |\boldsymbol{p}_1|^2 + |\boldsymbol{p}_3|^2 - 2\boldsymbol{p}_1 \cdot \boldsymbol{p}_3 \\
&= |\boldsymbol{p}_1|^2 + |\boldsymbol{p}_3|^2 - 2|\boldsymbol{p}_1||\boldsymbol{p}_3|\cos\theta \\
&= |\boldsymbol{p}_1|^2 + |\boldsymbol{p}_3|^2 - 2|\boldsymbol{p}_1||\boldsymbol{p}_3|(1 - 2\sin^2\frac{\theta}{2}) \\
&= (|\boldsymbol{p}_1| - |\boldsymbol{p}_3|)^2 + 4|\boldsymbol{p}_1||\boldsymbol{p}_3|\sin^2\frac{\theta}{2},
\end{aligned}
\tag{86}
$$

where θ is the angle between the vectors $\boldsymbol{p}_1$ and $\boldsymbol{p}_3$.

The values used in Equation 35 are defined for angles in the *cm* frame $t_0 \equiv t(\theta_{cm} = 0)$ and $t_\pi \equiv t(\theta_{cm} = \pi)$. Using these values in Equation 86, one finds

$$
\begin{aligned}
t_0 &= (E_{1,cm} - E_{3,cm})^2 - (|\boldsymbol{p}_{1,cm}| - |\boldsymbol{p}_{3,cm}|)^2, \tag{87} \\
t_\pi &= (E_{1,cm} - E_{3,cm})^2 - (|\boldsymbol{p}_{1,cm}| + |\boldsymbol{p}_{3,cm}|)^2. \tag{88}
\end{aligned}
$$

Now, $E_{1,cm}$ and $E_{3,cm}$ need to be cast into functions of s and the masses of the particles.

$$
\begin{aligned}
s &\equiv (p_1 + p_2)^2 = (p_3 + p_4)^2. \tag{89} \\
\sqrt{s} &= E_{1,cm} + E_{2,cm} = E_{3,cm} + E_{4,cm}. \tag{90}
\end{aligned}
$$

Now, use the relations for the cm reference frame,

$$
\begin{aligned}
E_{1,cm}^2 &= \boldsymbol{p}_{1,cm}^2 + m_1^2, \tag{91} \\
E_{2,cm}^2 &= \boldsymbol{p}_{2,cm}^2 + m_2^2, \tag{92}
\end{aligned}
$$

along with $|\boldsymbol{p}_{1,cm}| = |\boldsymbol{p}_{2,cm}|$, to obtain

$$
\sqrt{s} = E_{1,cm} + \sqrt{E_{1,cm}^2 - m_1^2 + m_2^2}.
\tag{93}
$$

Squaring both sides and simplifying yields

$$
E_{1,cm} = \frac{s + m_1^2 - m_2^2}{2\sqrt{s}}.
\tag{94}
$$

21

By a similar process, the value for $E_{3,cm}$ is given as

$$E_{3,cm} = \frac{s + m_3^2 - m_4^2}{2\sqrt{s}}. \tag{95}$$

To complete the derivation, $|\boldsymbol{p}_{1,cm}|$ and $|\boldsymbol{p}_{3,cm}|$ need to be rewritten in terms of λ_{12}, λ_{34} and s. From Equation 90,

$$\begin{aligned} s &= (E_{1,cm} + E_{2,cm})^2 \\ &= E_{1,cm}^2 + E_{2,cm}^2 + 2E_{1,cm}E_{2,cm} \\ &= \boldsymbol{p}_{1,cm}^2 + m_1^2 + \boldsymbol{p}_{1,cm}^2 + m_2^2 + 2\sqrt{(\boldsymbol{p}_{1,cm}^2 + m_1^2)(\boldsymbol{p}_{1,cm}^2 + m_2^2)}, \end{aligned} \tag{96}$$

where we have used the fact that $|\boldsymbol{p}_{1,cm}| = |\boldsymbol{p}_{2,cm}|$. Simplifying Equation 96 gives

$$\begin{aligned} 4s\boldsymbol{p}_{1,cm}^2 &= (s - m_1^2 - m_2^2)^2 + 4m_1^2 m_2^2 \\ &= \lambda_{12}. \end{aligned} \tag{97}$$

Therefore,

$$|\boldsymbol{p}_{1,cm}| = \sqrt{\frac{\lambda_{12}}{4s}}. \tag{98}$$

By a similar process, the value of $|\boldsymbol{p}_{3,cm}|$ is given as:

$$|\boldsymbol{p}_{3,cm}| = \sqrt{\frac{\lambda_{34}}{4s}}. \tag{99}$$

Substituting Equations 94, 95, 98 and 99 into Equations 87 and 88 gives us the final results

$$t_0 = \frac{1}{4s}[(m_1^2 - m_2^2 - m_3^2 + m_4^2)^2 - (\sqrt{\lambda_{12}} - \sqrt{\lambda_{34}})^2] \tag{100}$$

$$t_\pi = \frac{1}{4s}[(m_1^2 - m_2^2 - m_3^2 + m_4^2)^2 - (\sqrt{\lambda_{12}} + \sqrt{\lambda_{34}})^2] \tag{101}$$

Appendix C   Figures of Model Comparison to Experimental Data
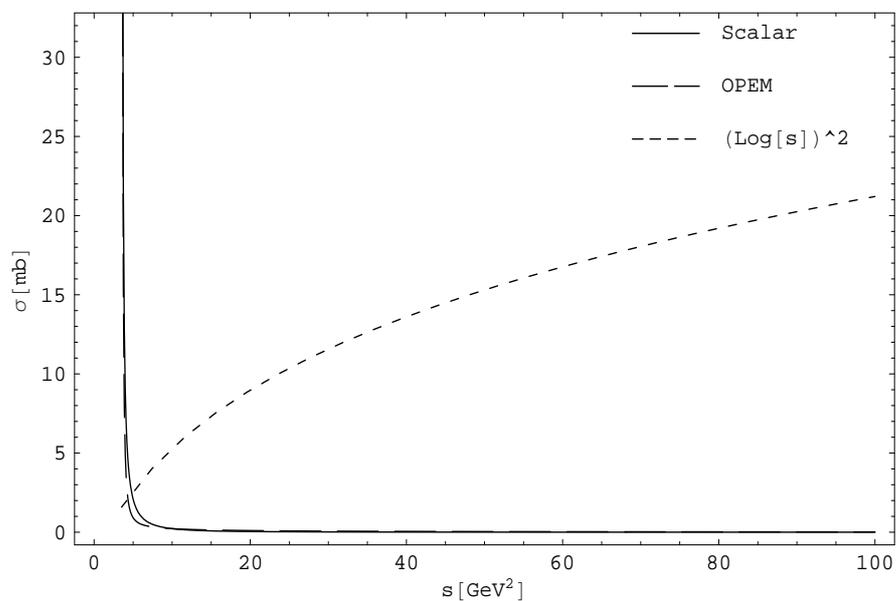
Figure 2: Comparison of the cross sections for the scalar theory and OPEM to the Froissart bound (Equation 68) [12]. Notice that the curves for the scalar theory and the OPEM lie almost on top of one another.
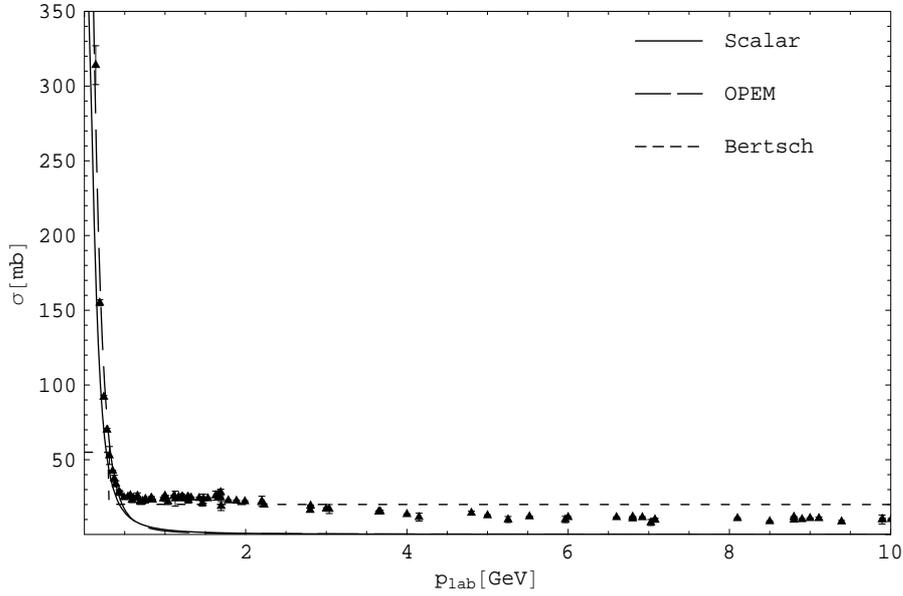
Figure 3: Comparison of the theoretical curves for OPEM, scalar theory and the parameterization of Bertsch [13] to data from the Particle Data Group [14] in the lab momentum range of $p_{lab} = 0 - 10$ GeV.
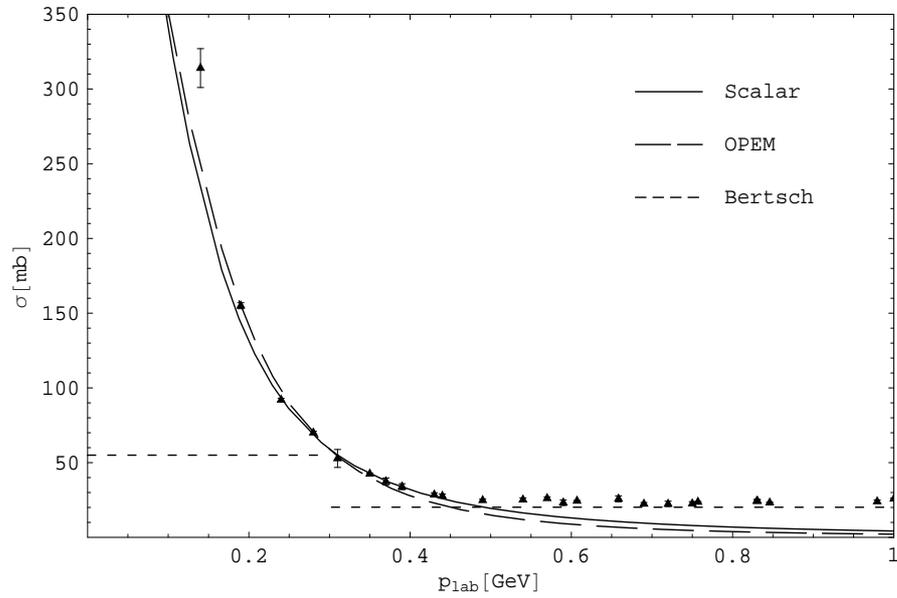
Figure 4: Comparison of the theoretical curves for OPEM, scalar theory and the parameterization of Bertsch [13] to data from the Particle Data Group [14] in the lab momentum range of $p_{lab} = 0 - 1$ GeV.
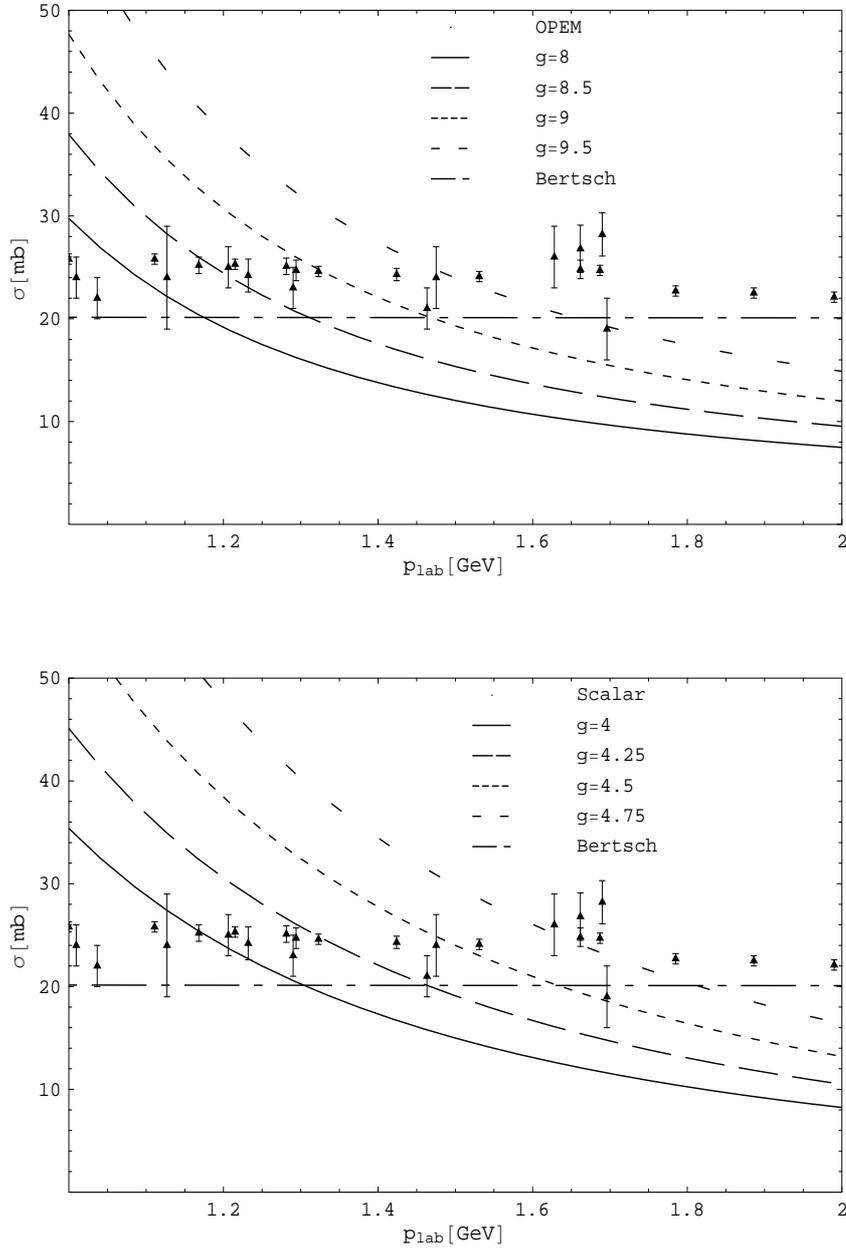
Figure 5: The OPEM (top) and the scalar theory (bottom) versus the parameterization of Bertsch [13] compared to data from the Particle Data Group [14] in the lab momentum range of $p_{lab} = 1 - 2$ GeV, for a variety of different coupling constants.

25
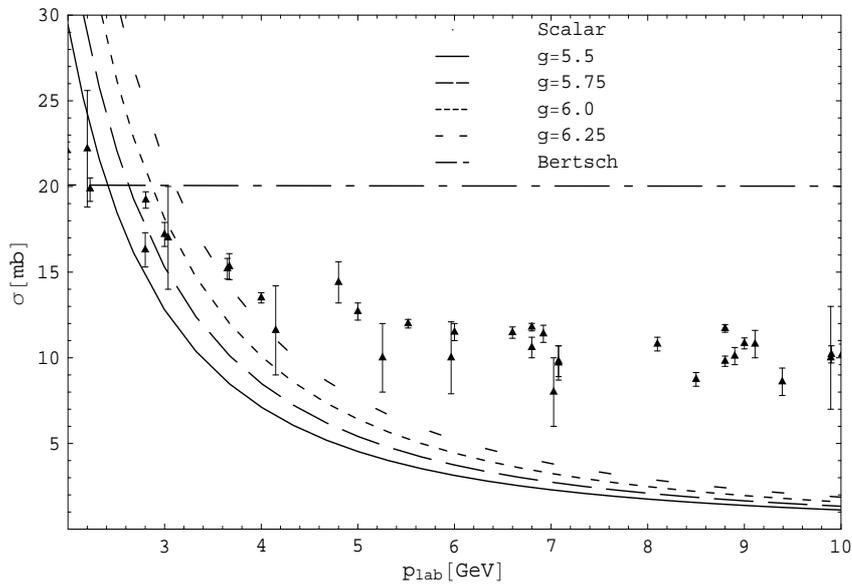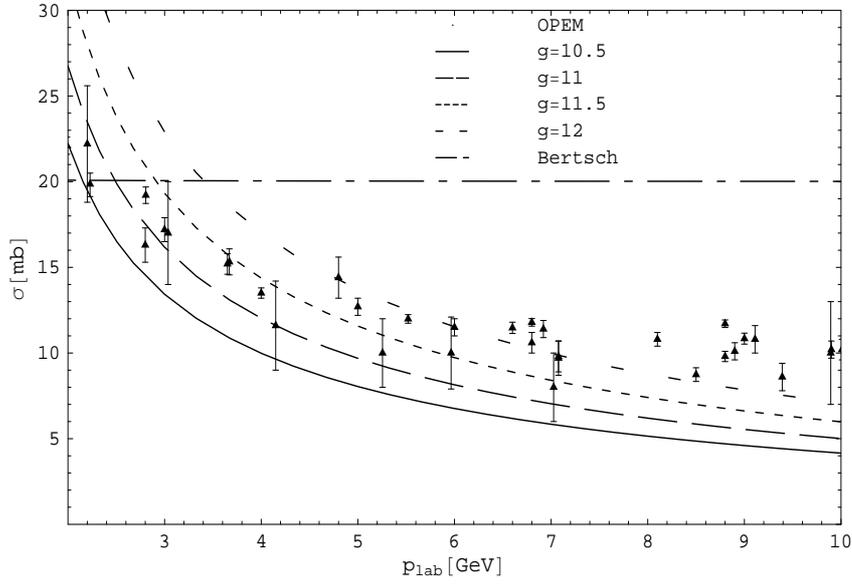
Figure 6: The OPEM (top) and the scalar theory (bottom) versus the parameterization of Bertsch [13] compared to data from the Particle Data Group [14] in the lab momentum range of $p_{lab} = 2 - 10$ GeV, for a variety of different coupling constants.

26
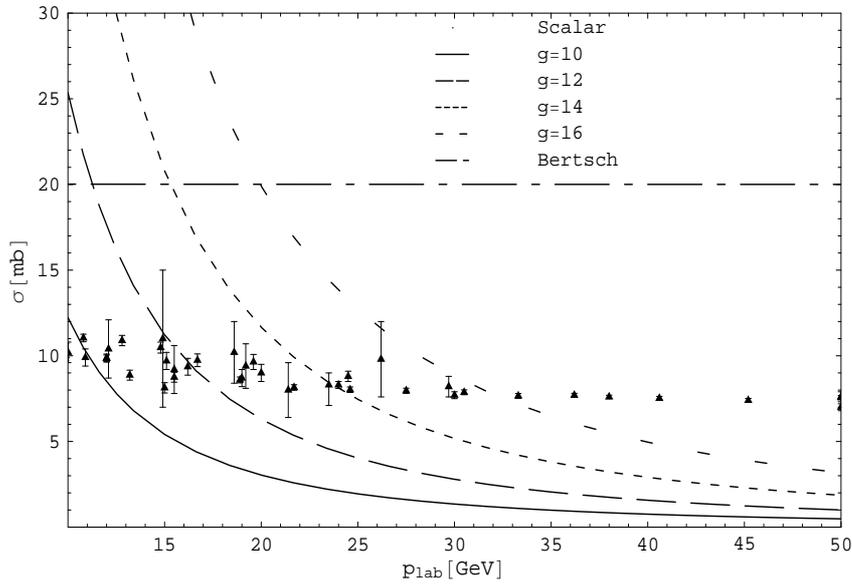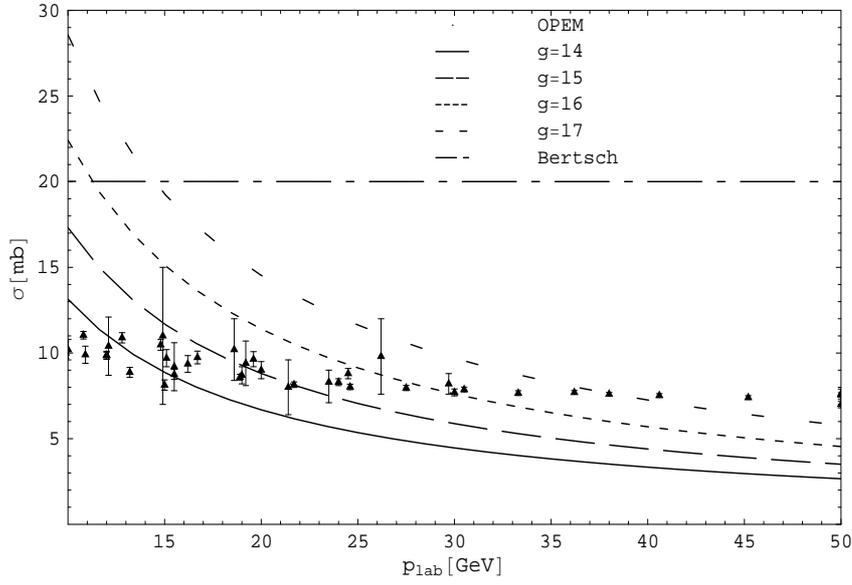
Figure 7: The OPEM (top) and the scalar theory (bottom) versus the parameterization of Bertsch [13] compared to data from the Particle Data Group [14] in the lab momentum range of $p_{lab} = 10 - 50$ GeV, for a variety of different coupling constants.

27
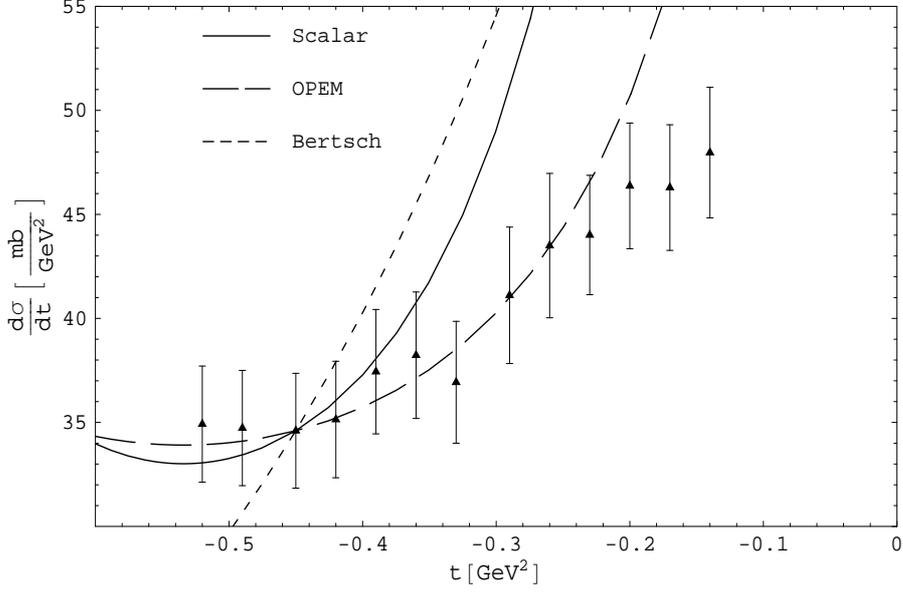
Figure 8: The OPEM ($g_{\pi NN} = 6.740$), scalar theory ($g = 7.515$ GeV) and the parameterization of Bertsch ($a = 135.7$ mb/GeV^2) [13] compared to data from Albrow et al. [15] at $p_{lab} = 1.18$ GeV.
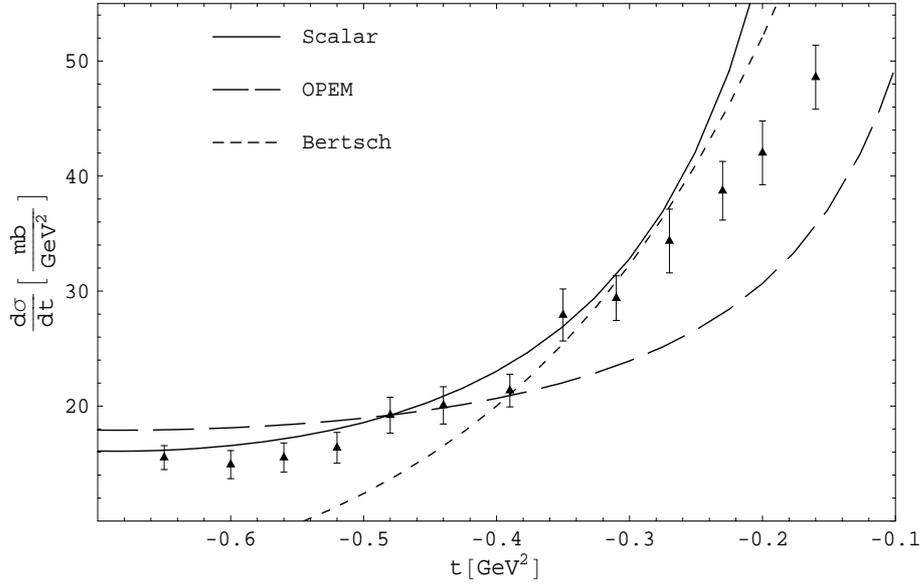
Figure 9: The OPEM ($g_{\pi NN} = 6.868$), scalar theory ($g = 7.662$ GeV) and the parameterization of Bertsch ($a = 135.7$ mb/GeV^2) [13] compared to data from Albrow et al. [15] at $p_{lab} = 1.38$ GeV.

28
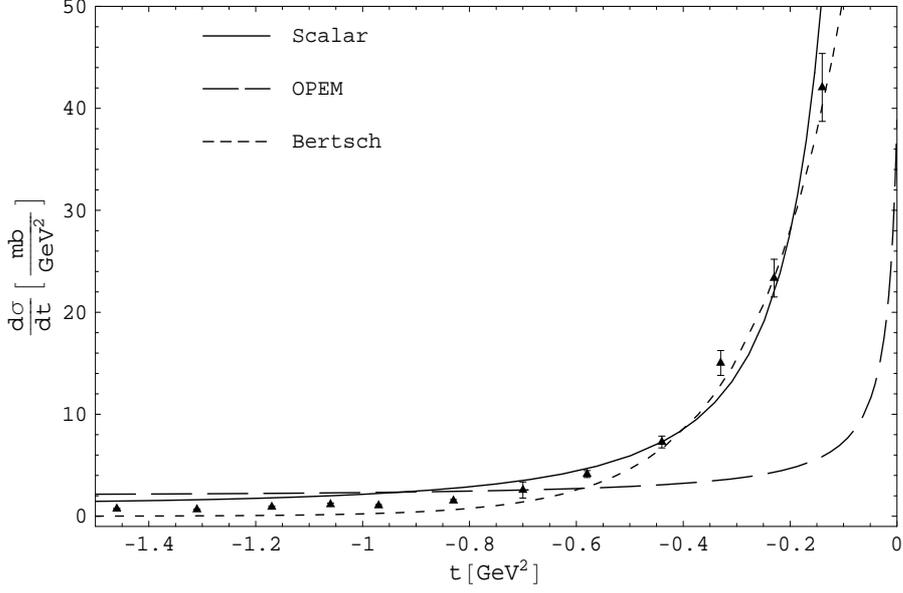
Figure 10: The OPEM ($g_{\pi NN} = 7.529$), scalar theory ($g = 9.463$ GeV) and the parameterization of Bertsch ($a = 98.62$ mb/GeV^2) [13] compared to data from Albrow et al. [15] at $p_{lab} = 2.74$ GeV.
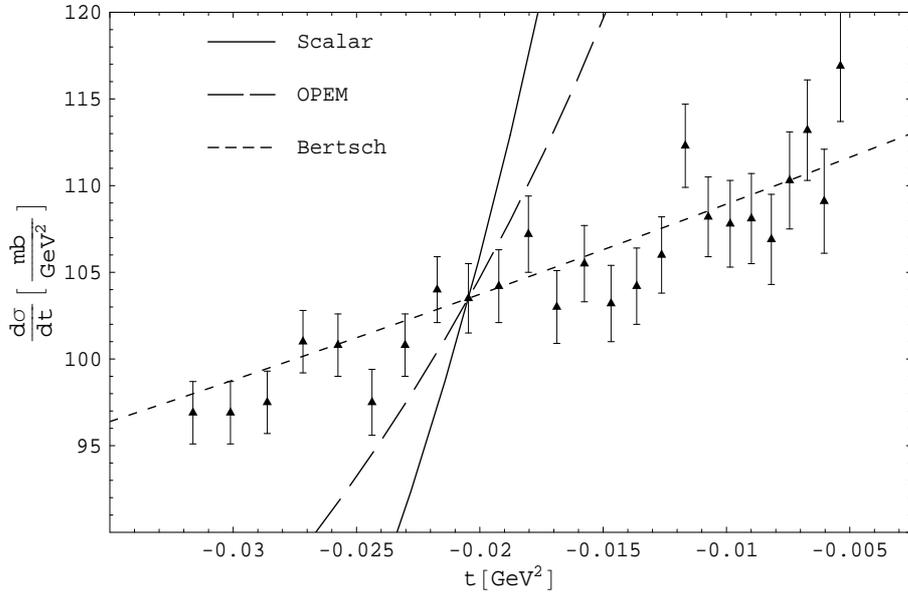
Figure 11: The OPEM ($g_{\pi NN} = 6.499$), scalar theory ($g = 4.020$ GeV) and the parameterization of Bertsch ($a = 114.4$ mb/GeV^2) [13] compared to data from Dobrovolsky et al. [16] at $p_{lab} = 1.399$ GeV.

29
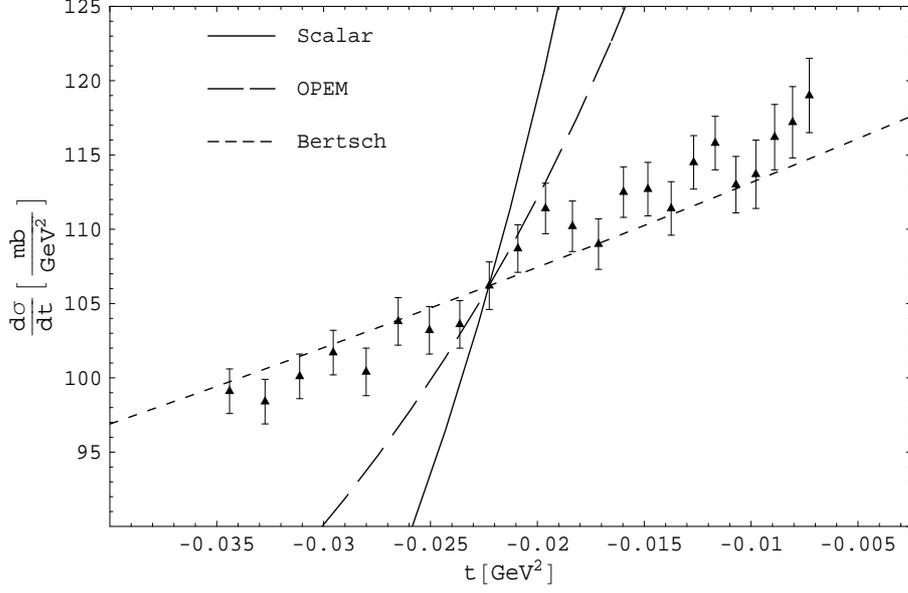
Figure 12: The OPEM ($g_{\pi NN} = 6.852$), scalar theory ($g = 4.224$ GeV) and the parameterization of Bertsch ($a = 119.2$ mb/GeV^2) [13] compared to data from Dobrovolsky et al. [16] at $p_{lab} = 1.457$ GeV.
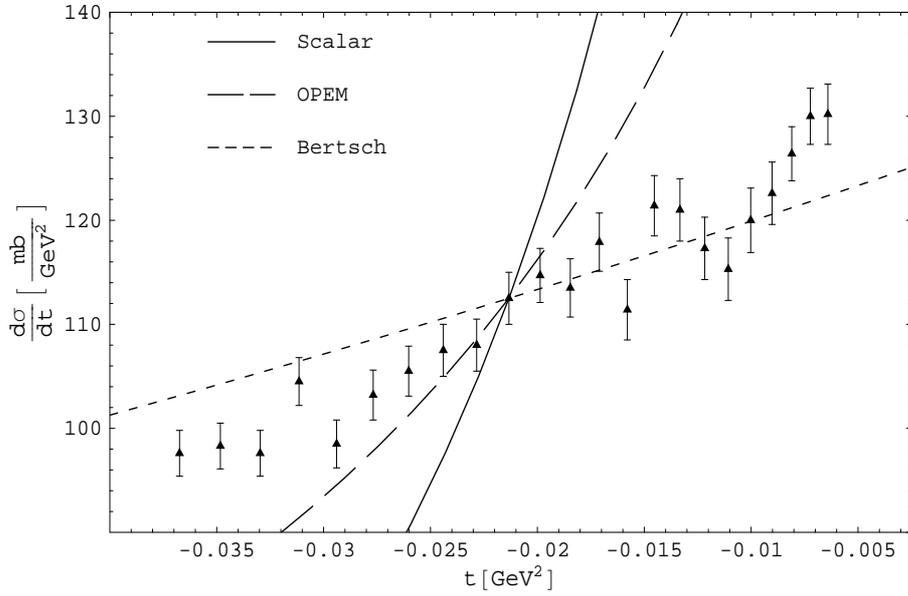

Figure 13: The OPEM ($g_{\pi NN} = 7.621$), scalar theory ($g = 4.490$ GeV) and the parameterization of Bertsch ($a = 126.9$ mb/GeV^2) [13] compared to data from Dobrovolsky et al. [16] at $p_{lab} = 1.629$ GeV.
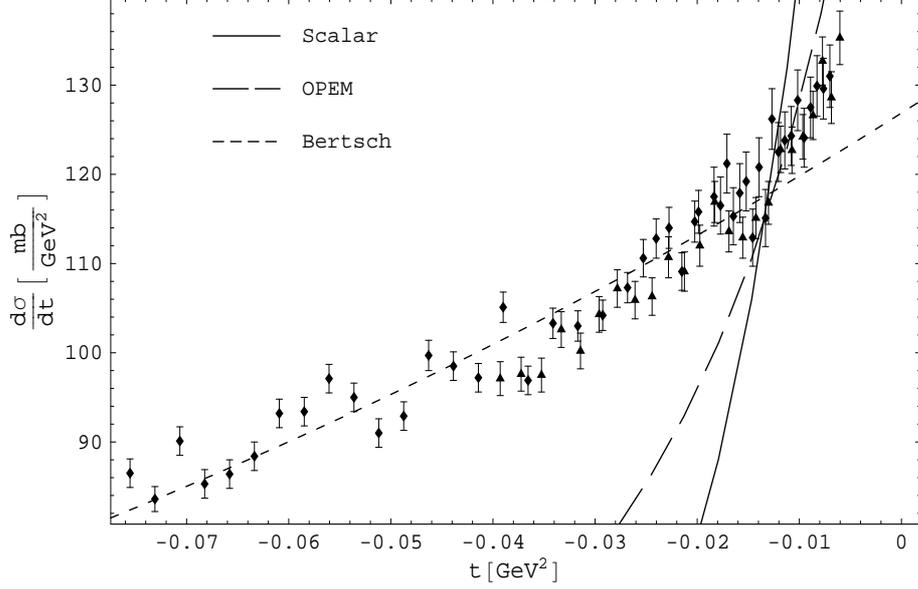
Figure 14: The OPEM ($g_{\pi NN} = 7.482$), scalar theory ($g = 4.113$ GeV) and the parameterization of Bertsch ($a = 126.9$ mb/GeV^2) [13] compared to data from Dobrovolsky et al. [16] at $p_{lab} = 1.686$ GeV.
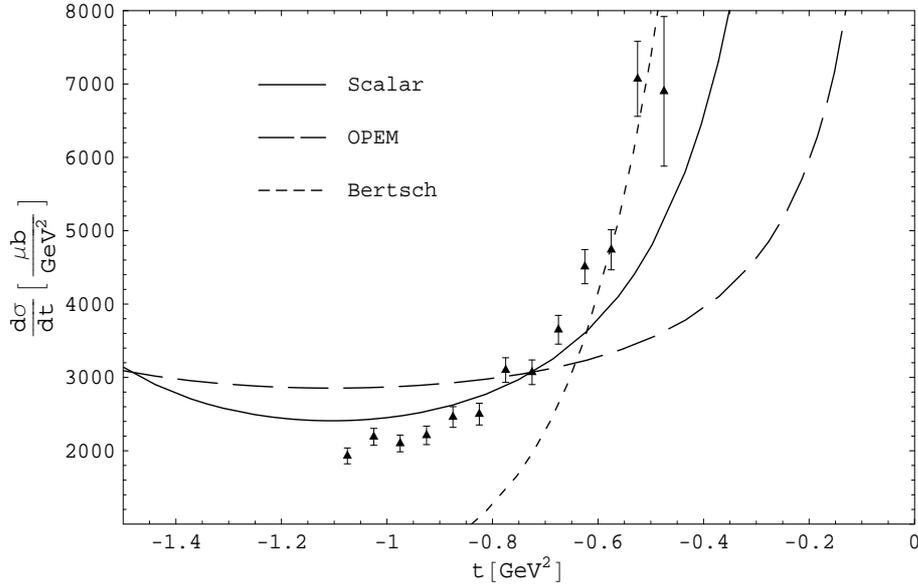

Figure 15: The OPEM ($g_{\pi NN} = 5.988$), scalar theory ($g = 7.058$ GeV) and the parameterization of Bertsch ($a = 139.5$ mb/GeV^2) [13] compared to data from Jenkins et al. [17] at $p_{lab} = 1.896$ GeV.

31
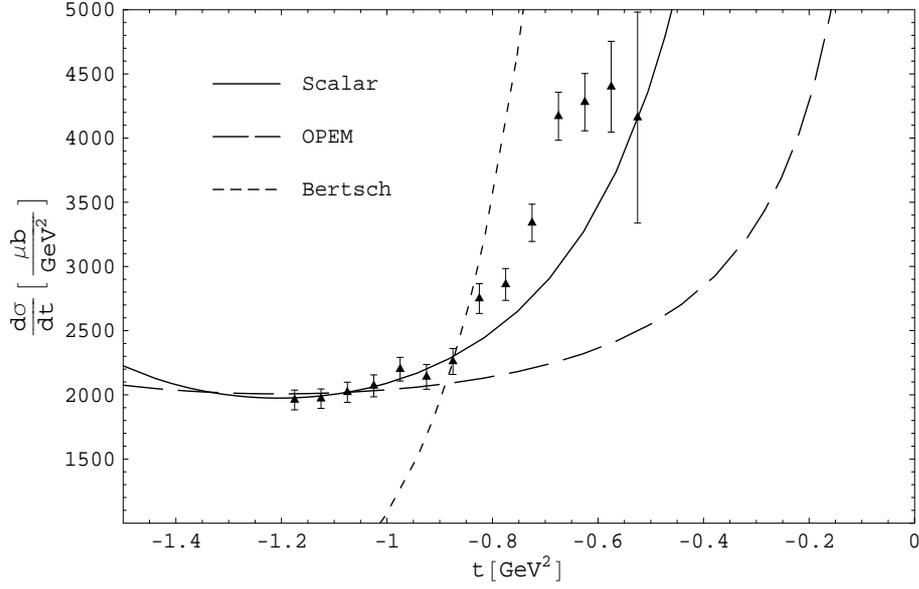
Figure 16: The OPEM ($g_{\pi NN} = 5.793$), scalar theory ($g = 7.227$ GeV) and the parameterization of Bertsch ($a = 403.3$ mb/GeV^2) [13] compared to data from Jenkins et al. [17] at $p_{lab} = 2.015$ GeV.
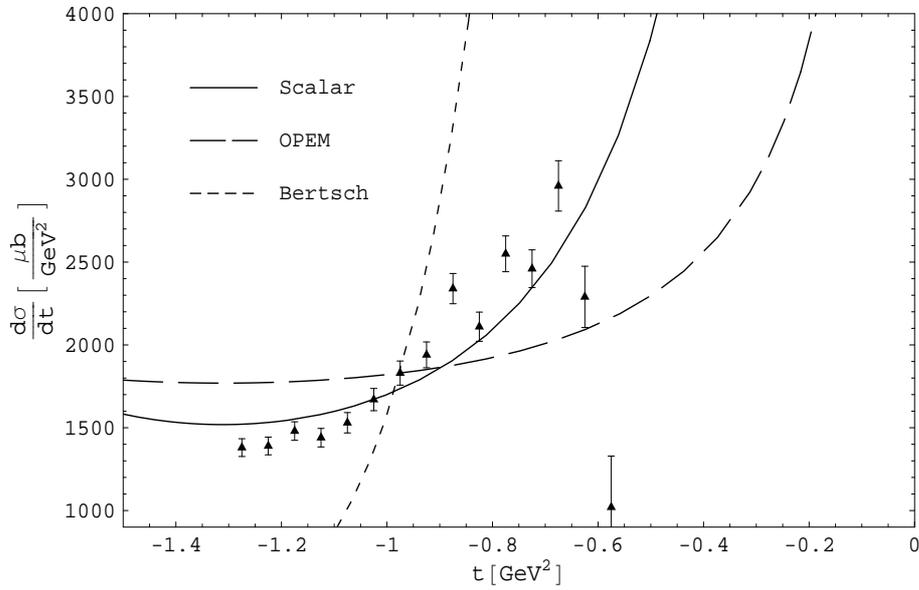

Figure 17: The OPEM ($g_{\pi NN} = 5.912$), scalar theory ($g = 7.269$ GeV) and the parameterization of Bertsch ($a = 606.0$ mb/GeV^2) [13] compared to data from Jenkins et al. [17] at $p_{lab} = 2.139$ GeV.
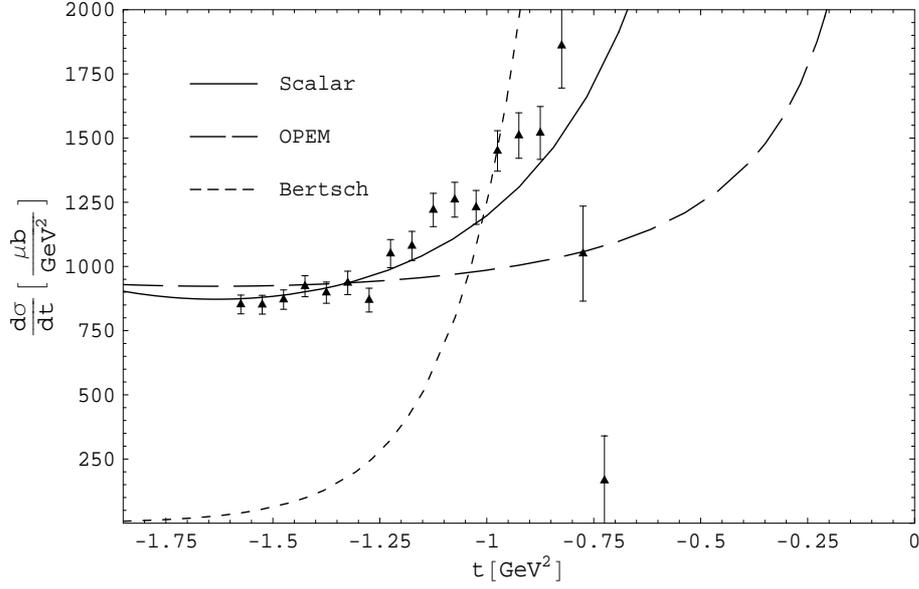
Figure 18: The OPEM ($g_{\pi NN} = 5.714$), scalar theory ($g = 7.634$ GeV) and the parameterization of Bertsch ($a = 495.7$ mb/GeV^2) [13] compared to data from Jenkins et al. [17] at $p_{lab} = 2.508$ GeV.
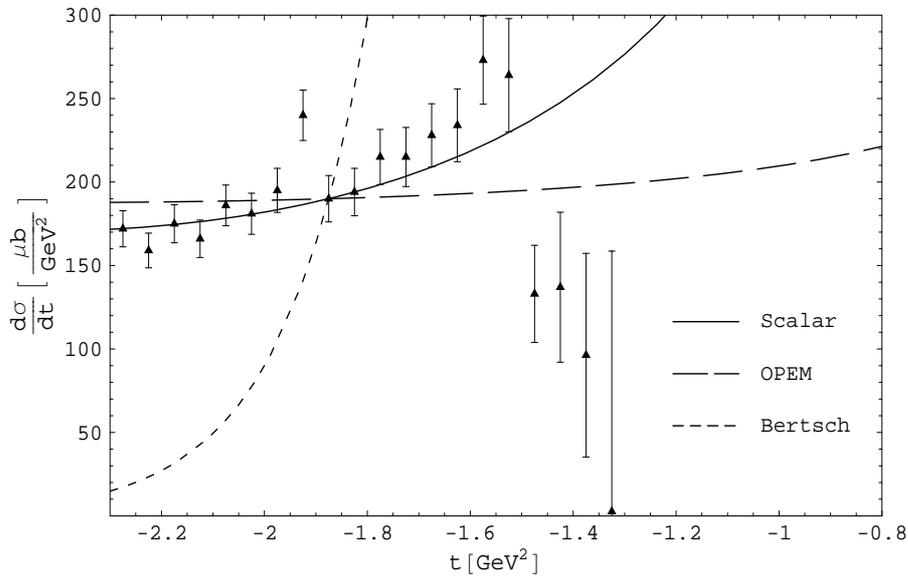

Figure 19: The OPEM ($g_{\pi NN} = 4.760$), scalar theory ($g = 7.222$ GeV) and the parameterization of Bertsch ($a = 14550$ mb/GeV^2) [13] compared to data from Jenkins et al. [17] at $p_{lab} = 3.410$ GeV.
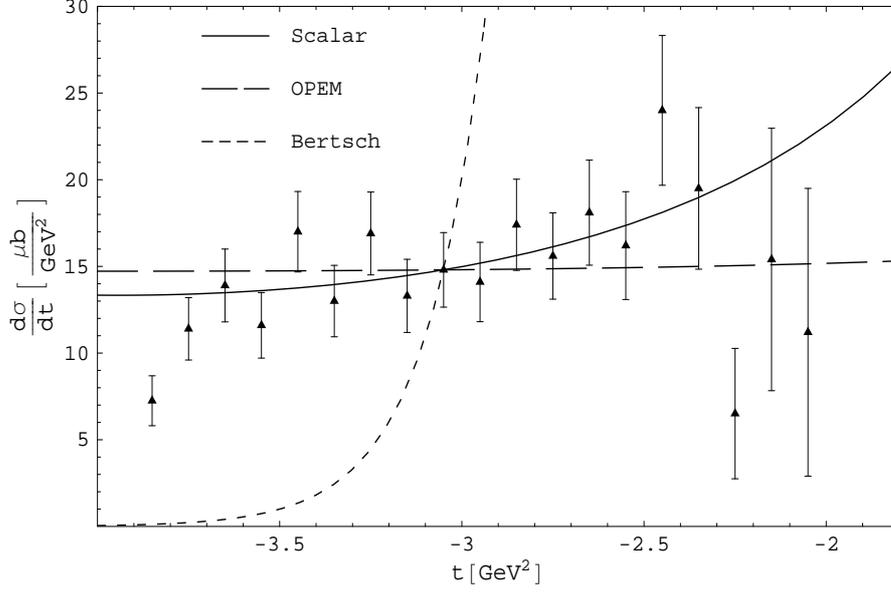
Figure 20: The OPEM ($g_{\pi NN} = 3.186$), scalar theory ($g = 5.94$ GeV) and the parameterization of Bertsch ($a = 1.31 \times 10^6$ mb/GeV^2) [13] compared to data from Jenkins et al. [17] at $p_{lab} = 5.055$ GeV.
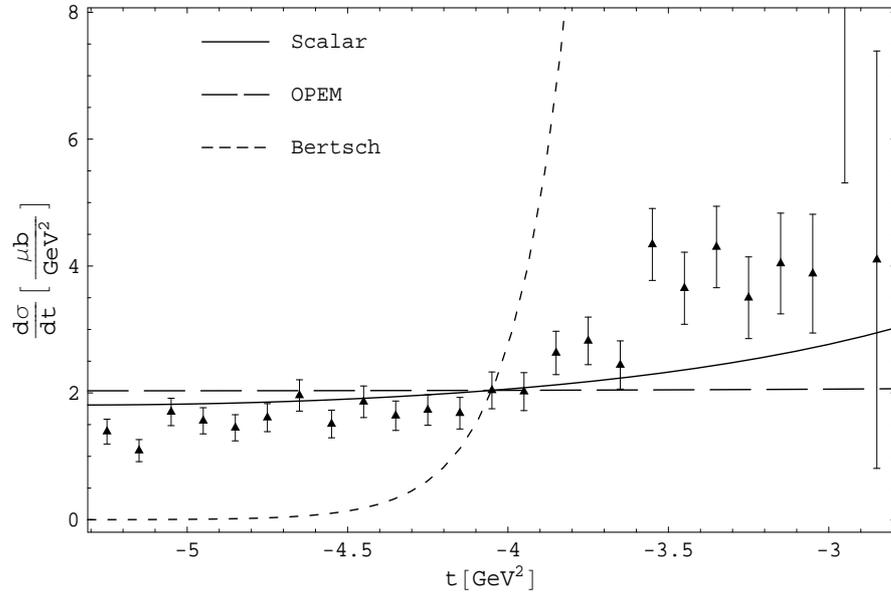
Figure 21: The OPEM ($g_{\pi NN} = 2.240$), scalar theory ($g = 4.754$ GeV) and the parameterization of Bertsch ($a = 7.29 \times 10^6$ mb/GeV^2) [13] compared to data from Jenkins et al. [17] at $p_{lab} = 6.57$ GeV.
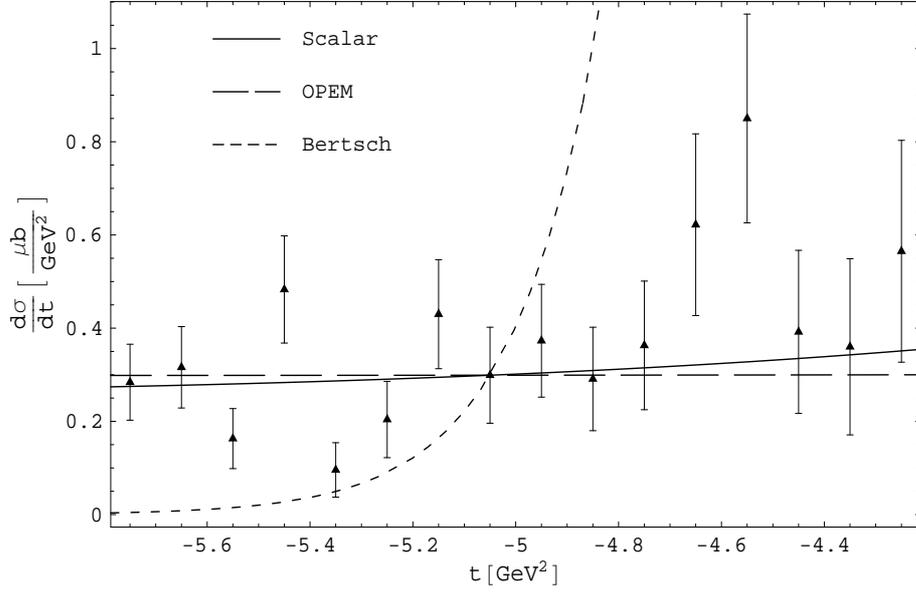
Figure 22: The OPEM ($g_{\pi NN} = 1.540$), scalar theory ($g = 3.633$ GeV) and the parameterization of Bertsch ($a = 4.31 \times 10^9$ mb/GeV^2) [13] compared to data from Jenkins et al. [17] at $p_{lab} = 8.022$ GeV.
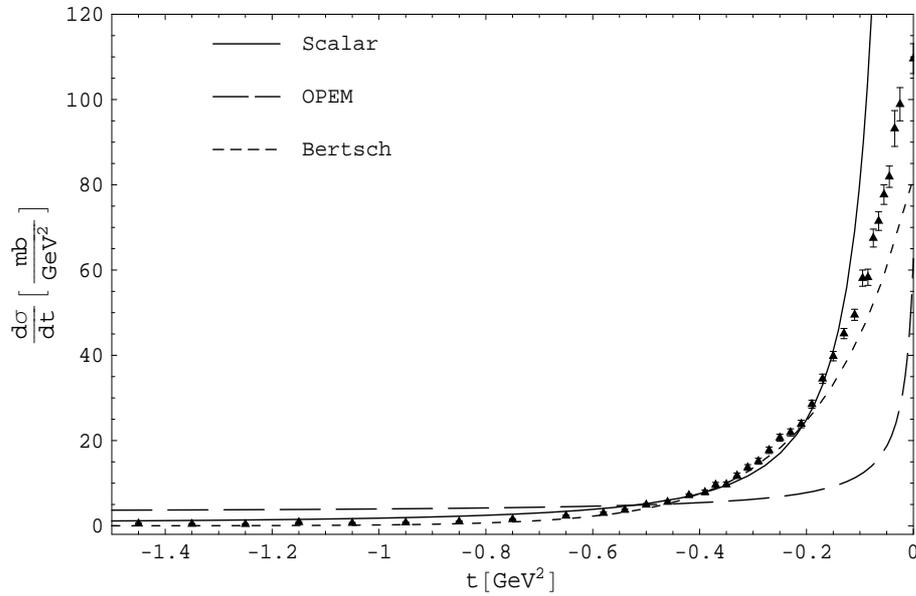

Figure 23: The OPEM ($g_{\pi NN} = 9.141$), scalar theory ($g = 9.668$ GeV) and the parameterization of Bertsch ($a = 81.53$ mb/GeV^2) [13] compared to data from Ambats et al. [18] at $p_{lab} = 3.00$ GeV.
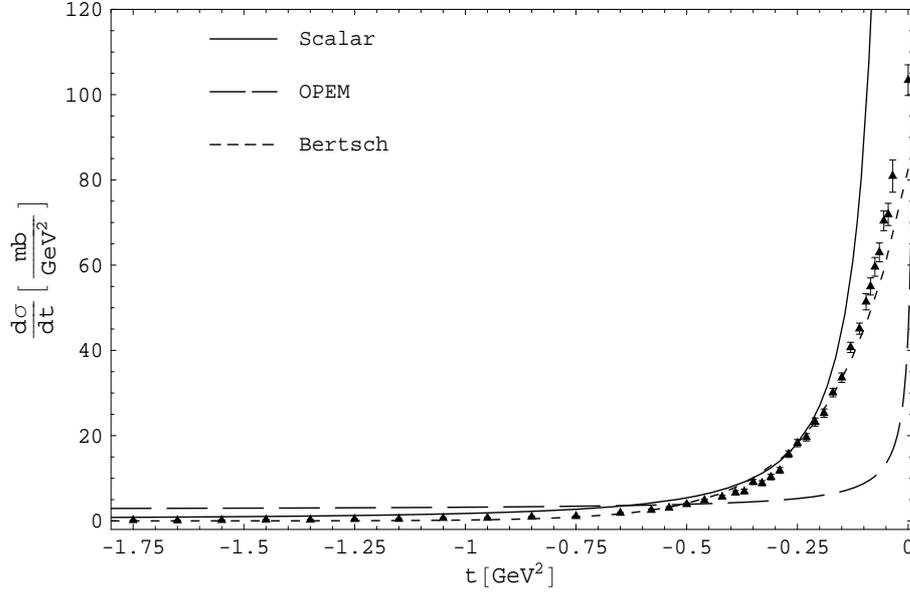
Figure 24: The OPEM ($g_{\pi NN} = 9.821$), scalar theory ($g = 10.94$ GeV) and the parameterization of Bertsch ($a = 81.73$ mb/GeV^2) [13] compared to data from Ambats et al. [18] at $p_{lab} = 3.65$ GeV.
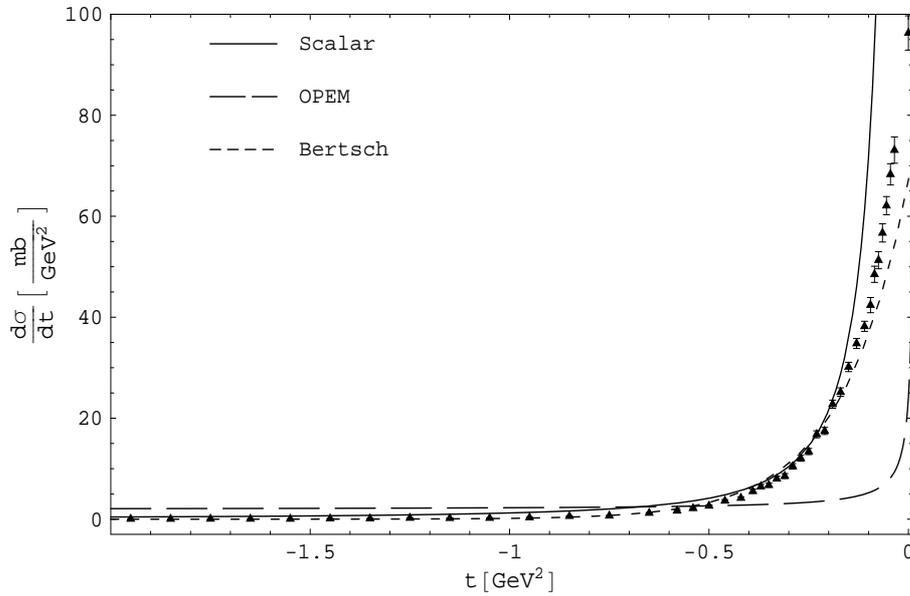

Figure 25: The OPEM ($g_{\pi NN} = 10.85$), scalar theory ($g = 12.19$ GeV) and the parameterization of Bertsch ($a = 66.87$ mb/GeV^2) [13] compared to data from Ambats et al. [18] at $p_{lab} = 5.00$ GeV.
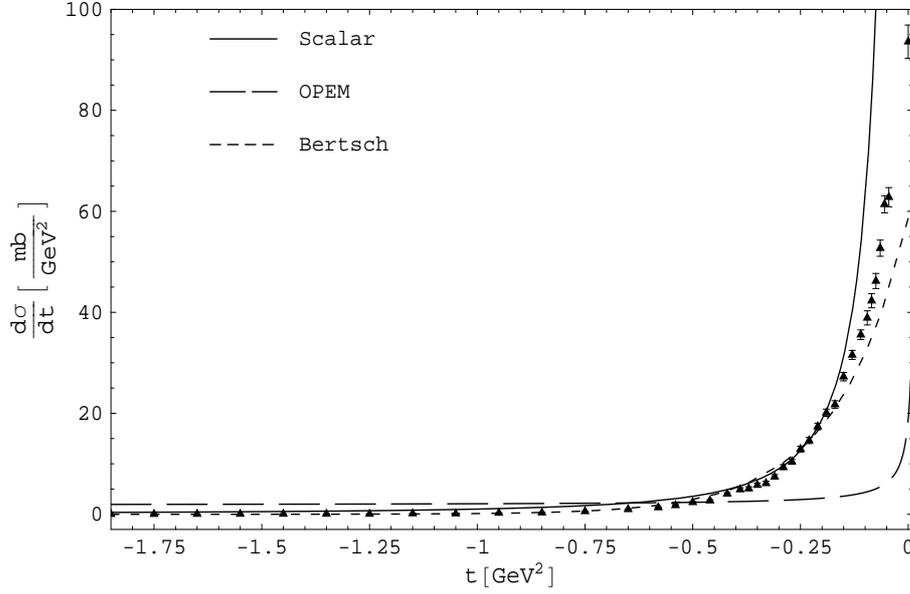
Figure 26: The OPEM ($g_{\pi NN} = 11.77$), scalar theory ($g = 12.93$ GeV) and the parameterization of Bertsch ($a = 58.08$ mb/GeV^2) [13] compared to data from Ambats et al. [18] at $p_{lab} = 6.00$ GeV.
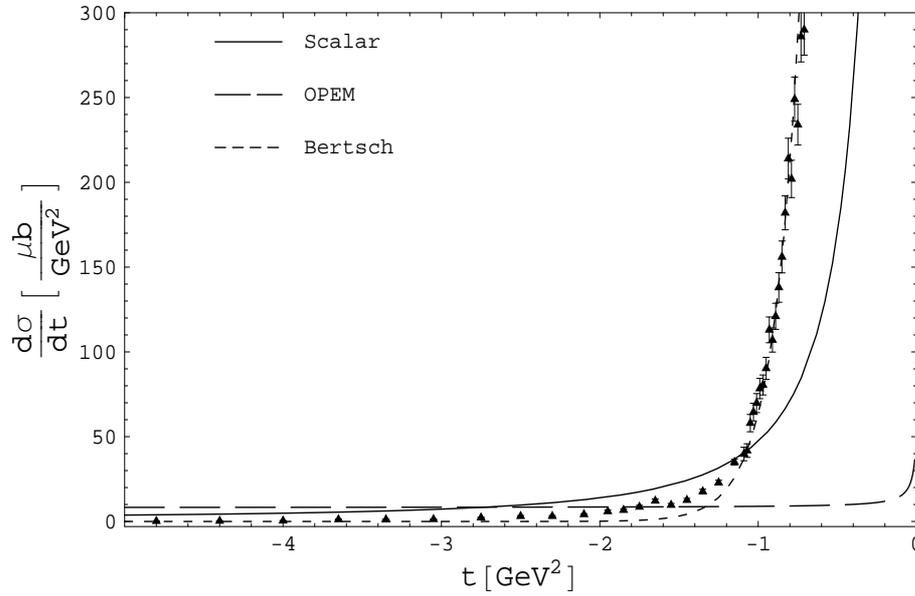
Figure 27: The OPEM ($g_{\pi NN} = 3.751$), scalar theory ($g = 7.489$ GeV) and the parameterization of Bertsch ($a = 25.67$ mb/GeV^2) [13] compared to data from Baglin et al. [19] at $p_{lab} = 9.0$ GeV.
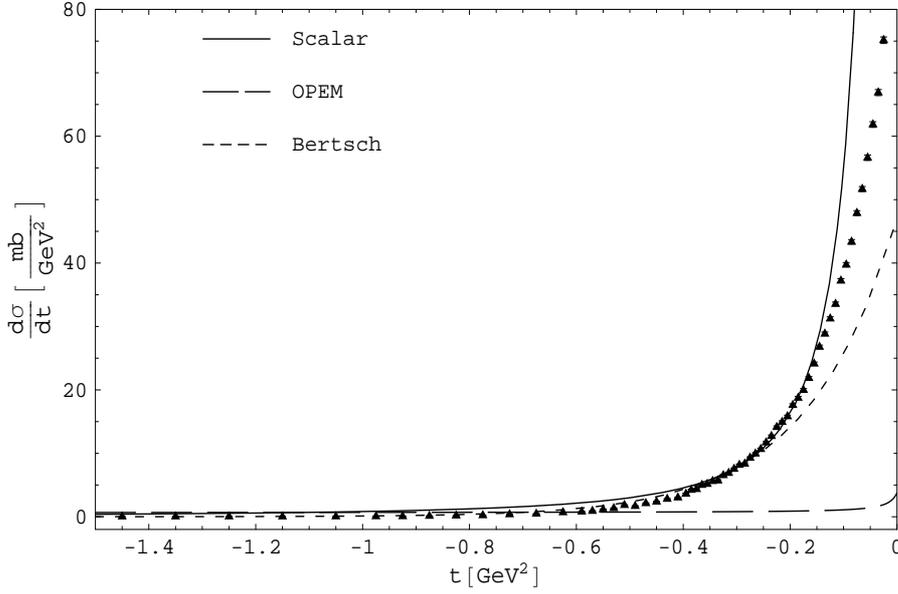
Figure 28: The OPEM ($g_{\pi NN} = 12.00$), scalar theory ($g = 16.52$ GeV) and the parameterization of Bertsch ($a = 46.87$ mb/GeV^2) [13] compared to data from Brandenburg et al. [20] at $p_{lab} = 10.4$ GeV.
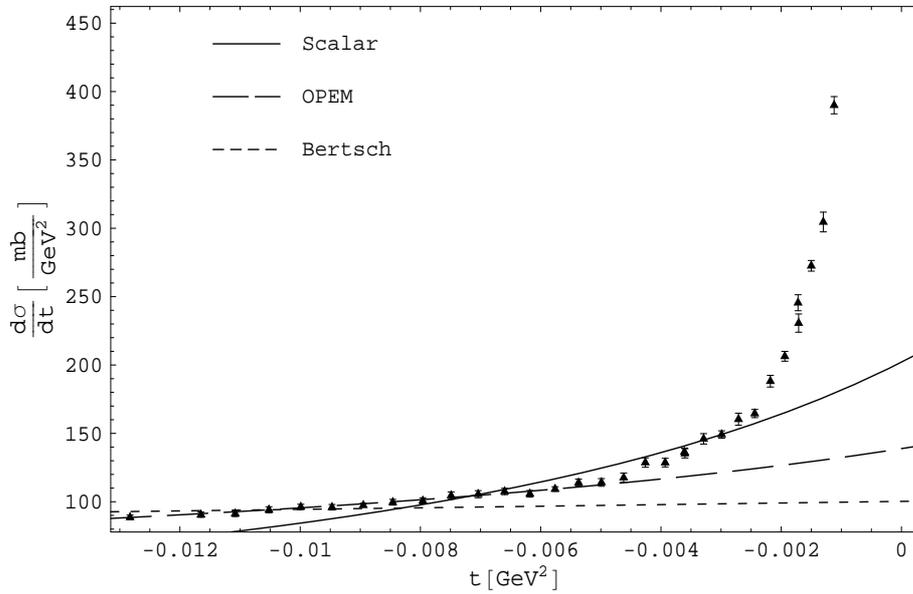

Figure 29: The OPEM ($g_{\pi NN} = 27.45$), scalar theory ($g = 8.578$ GeV) and the parameterization of Bertsch ($a = 100.3$ mb/GeV^2) [13] compared to data from Beznogikh et al. [21] at $p_{lab} = 9.43$ GeV.

38
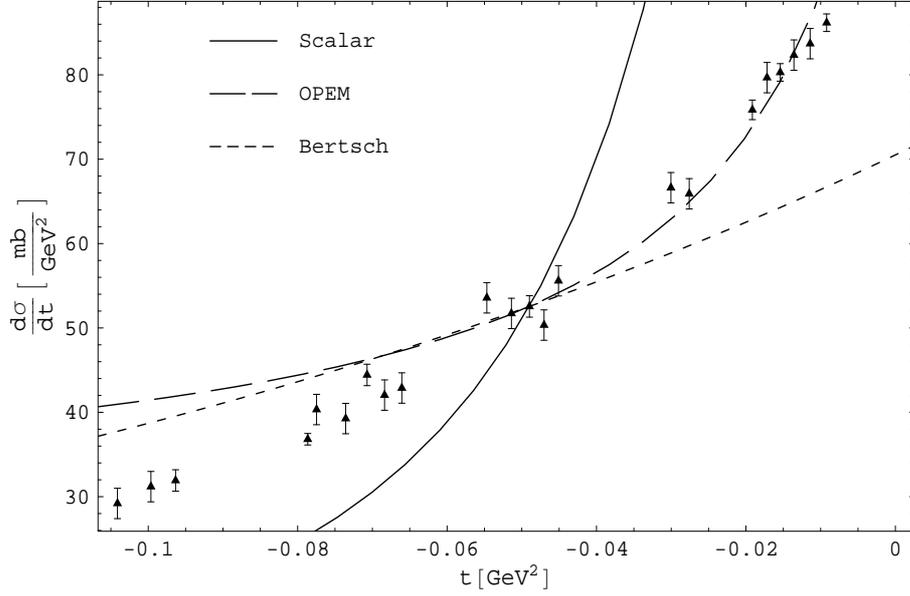
Figure 30: The OPEM ($g_{\pi NN} = 34.54$), scalar theory ($g = 13.88$ GeV) and the parameterization of Bertsch ($a = 70.49$ mb/GeV^2) [13] compared to data from Beznogikh et al. [21] at $p_{lab} = 13.16$ GeV.
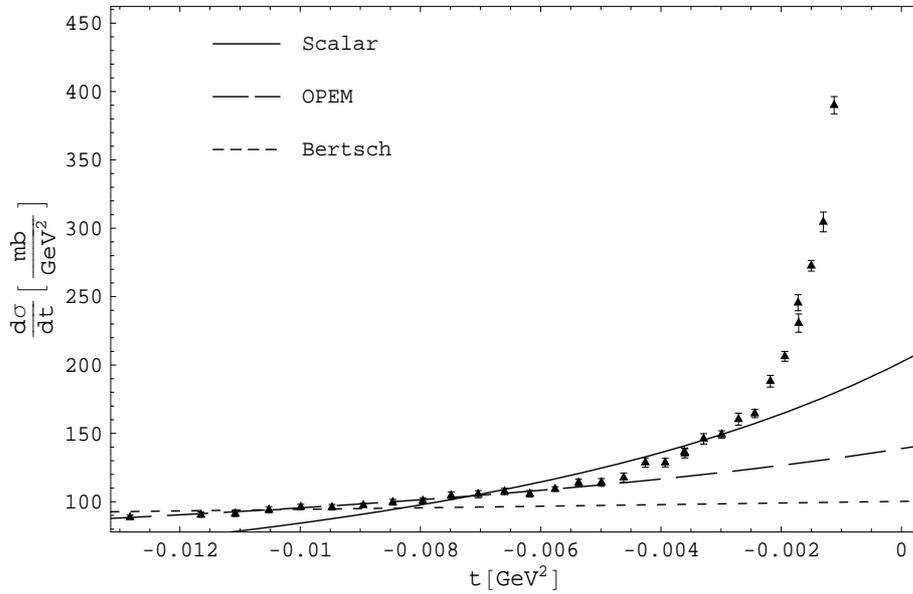
Figure 31: The OPEM ($g_{\pi NN} = 38.32$), scalar theory ($g = 15.36$ GeV) and the parameterization of Bertsch ($a = 69.13$ mb/GeV^2) [13] compared to data from Beznogikh et al. [21] at $p_{lab} = 15.52$ GeV.
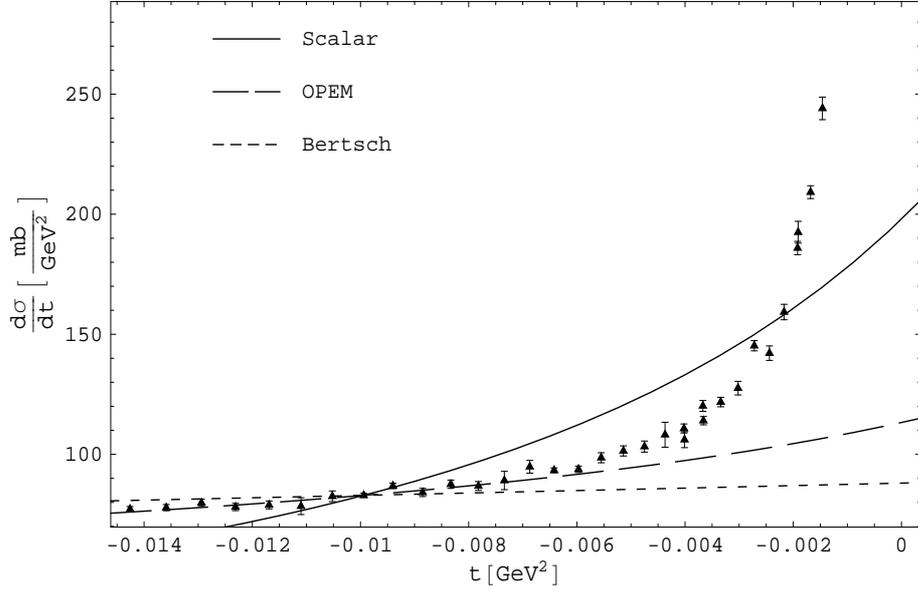
Figure 32: The OPEM ($g_{\pi NN} = 44.44$), scalar theory ($g = 12.19$ GeV) and the parameterization of Bertsch ($a = 89.03$ mb/GeV^2) [13] compared to data from Beznogikh et al. [21] at $p_{lab} = 19.23$ GeV.
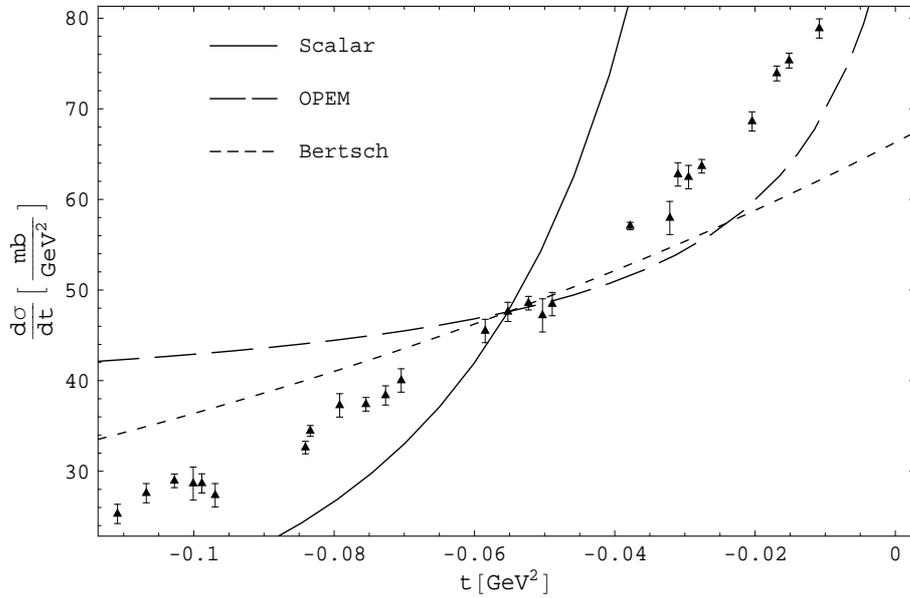

Figure 33: The OPEM ($g_{\pi NN} = 50.54$), scalar theory ($g = 19.36$ GeV) and the parameterization of Bertsch ($a = 66.29$ mb/GeV^2) [13] compared to data from Beznogikh et al. [21] at $p_{lab} = 24.56$ GeV.
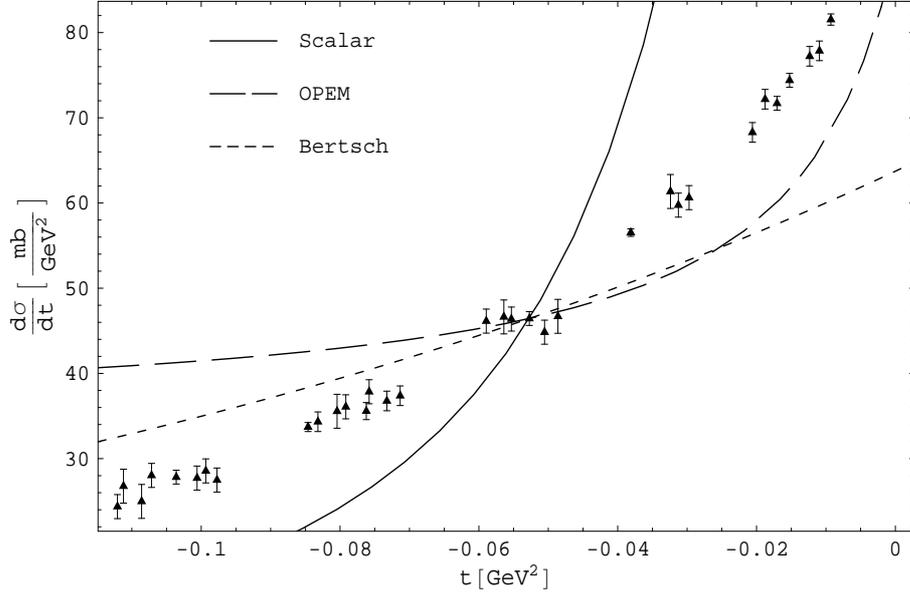
Figure 34: The OPEM ($g_{\pi NN} = 50.07$), scalar theory ($g = 18.90$ GeV) and the parameterization of Bertsch ($a = 63.72$ mb/GeV^2) [13] compared to data from Beznogikh et al. [21] at $p_{lab} = 27.53$ GeV.
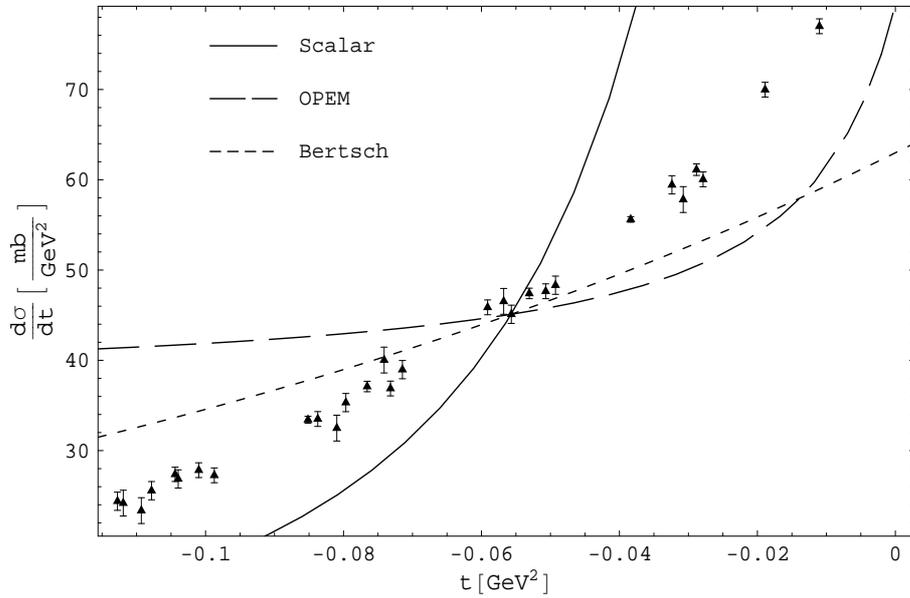

Figure 35: The OPEM ($g_{\pi NN} = 56.77$), scalar theory ($g = 21.34$ GeV) and the parameterization of Bertsch ($a = 62.98$ mb/GeV^2) [13] compared to data from Beznogikh et al. [21] at $p_{lab} = 30.45$ GeV.
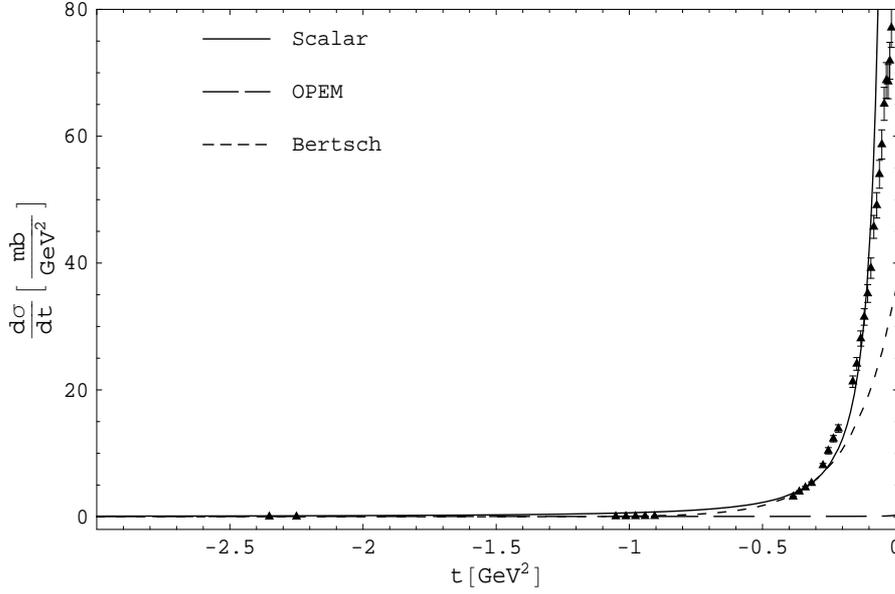
Figure 36: The OPEM ($g_{\pi NN} = 6.042$), scalar theory ($g = 15.01$ GeV) and the parameterization of Bertsch ($a = 35.29$ mb/GeV^2) [13] compared to data from Edelstein et al. [22] at $p_{lab} = 9.900$ GeV.
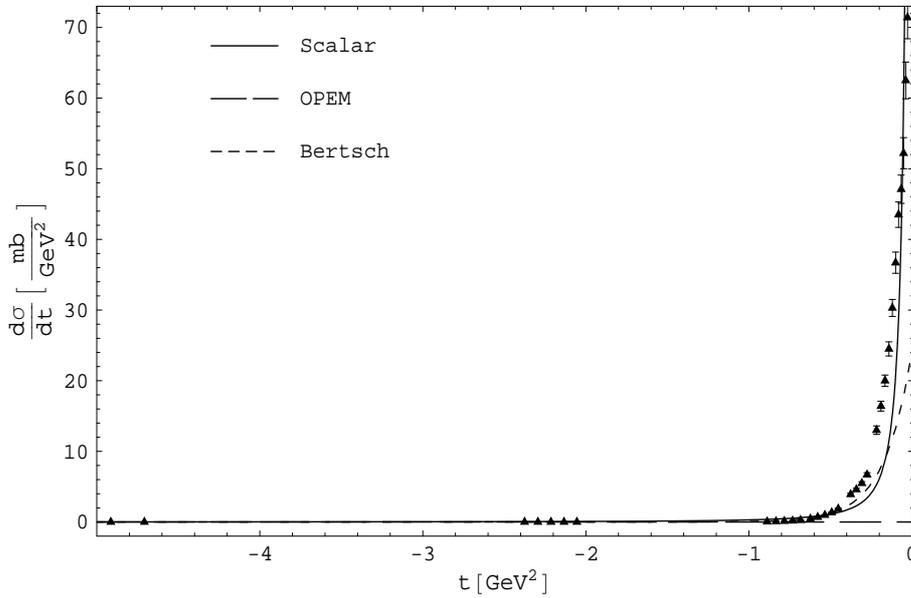

Figure 37: The OPEM ($g_{\pi NN} = 3.617$), scalar theory ($g = 15.61$ GeV) and the parameterization of Bertsch ($a = 24.14$ mb/GeV^2) [13] compared to data from Edelstein et al. [22] at $p_{lab} = 15.100$ GeV.
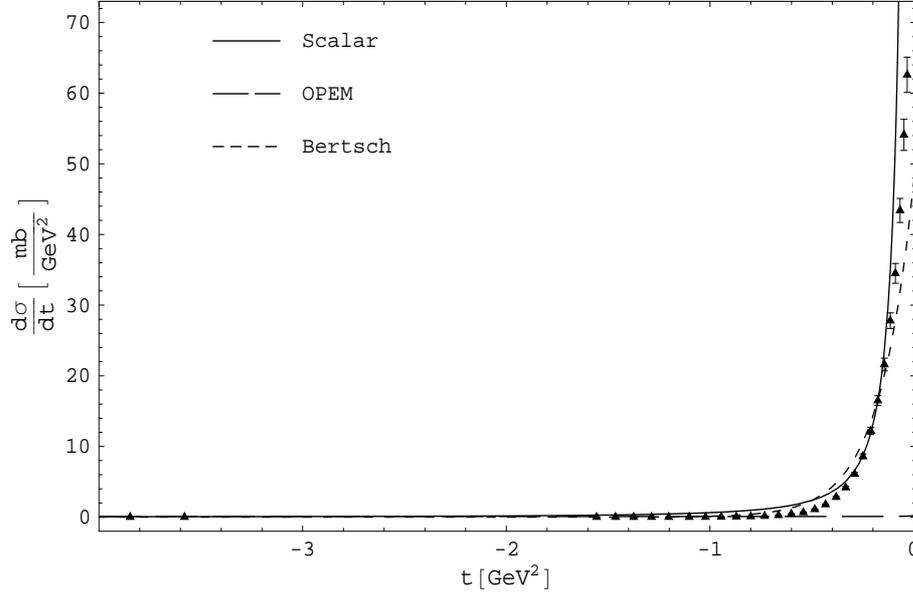
Figure 38: The OPEM ($g_{\pi NN} = 9.975$), scalar theory ($g = 21.76$ GeV) and the parameterization of Bertsch ($a = 47.42$ mb/GeV^2) [13] compared to data from Edelstein et al. [22] at $p_{lab} = 20.000$ GeV.
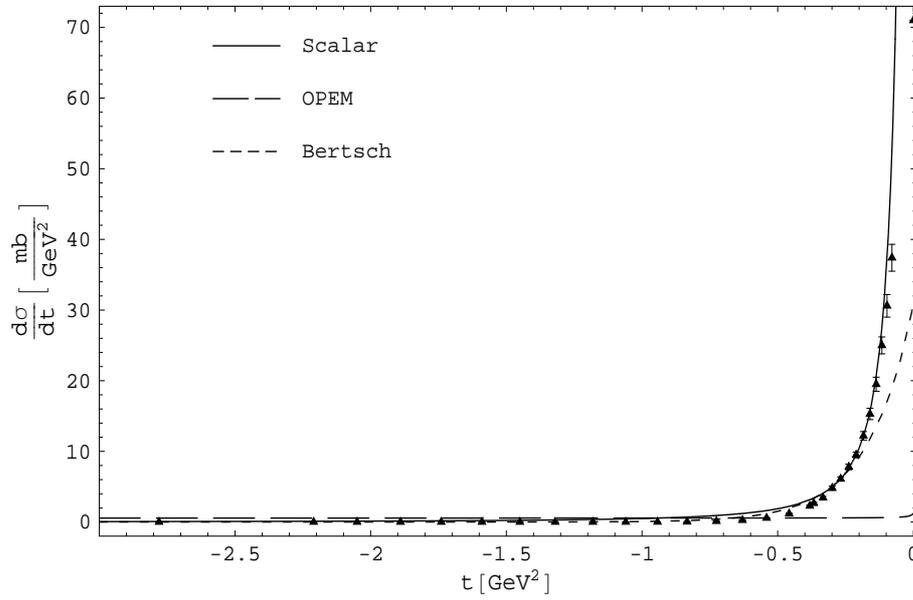

Figure 39: The OPEM ($g_{\pi NN} = 19.62$), scalar theory ($g = 25.10$ GeV) and the parameterization of Bertsch ($a = 30.45$ mb/GeV^2) [13] compared to data from Edelstein et al. [22] at $p_{lab} = 29.700$ GeV.
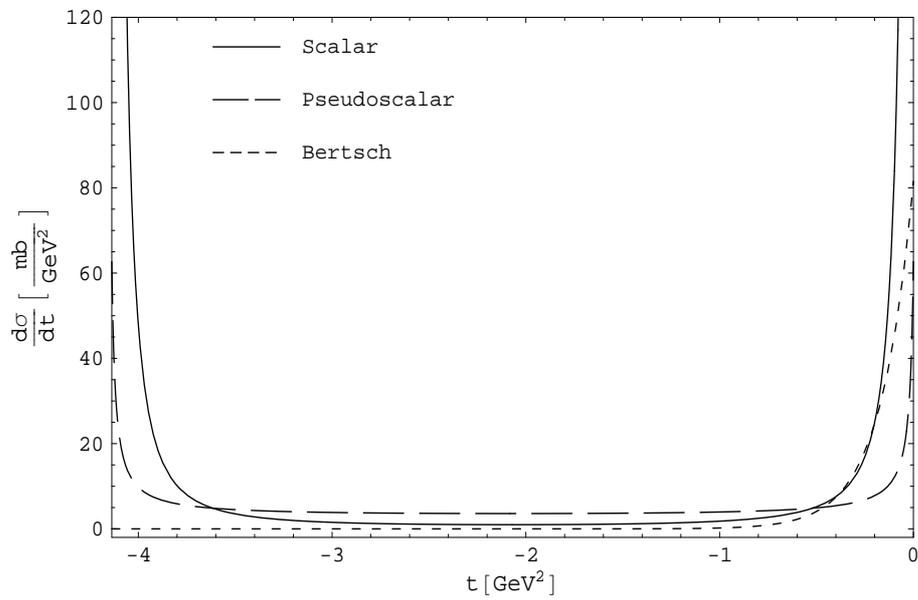
Figure 40: Comparison of the theoretical curves for OPEM, scalar theory and the parameterization of Bertsch [13] for the full physical range of t at $p_{lab} = 3.00$ GeV.

Appendix D   Experimental Data

Table 1: Data for Figure 3 through Figure 10 taken from the Particle Data Group [14]. Note that 1.0E+01 is defined as 1.0×10^1.

p_{lab} (GeV)	Max. p_{lab} (GeV)	Min. p_{lab} (GeV)	Experimental Cross Section (mb)	Stat. Error Max.(mb)	Stat. Error Min.(mb)	Systematic Error (+%)	Systematic Error (-%)
0.14	0.14	0.14	314	13	13	0	0
0.19	0.19	0.19	155	2	2	0	0
0.24	0.24	0.24	92	1	1	0	0
0.28	0.28	0.28	70	1	1	0	0
0.31	0.31	0.31	52.8	6	6	0	0
0.35	0.35	0.35	42.5	0.4	0.4	0	0
0.37	0.37	0.37	37.4	2.3	2.3	0	0
0.39	0.39	0.39	33.9	2	2	0	0
0.43	0.43	0.43	28.5	1.3	1.3	0	0
0.44	0.44	0.44	27.7	1.3	1.3	0	0
0.49	0.49	0.49	24.8	0.8	0.8	0	0
0.54	0.54	0.54	25.2	1.2	1.2	0	0
0.57	0.57	0.57	26.1	1	1	0	0
0.59	0.59	0.59	23.2	1.9	1.9	0	0
0.61	0.59	0.63	24.4	0.24	0.24	0	0
0.66	0.65	0.67	25.8	2	2	0	0
0.69	0.69	0.69	22.4	0.9	0.9	0	0
0.72	0.72	0.72	22.4	1.8	1.8	0	0
0.75	0.75	0.75	22.6	1.3	1.3	0	0
0.76	0.74	0.78	23.7	0.21	0.21	0	0
0.83	0.83	0.83	24.3	1	1	0	0
0.83	0.82	0.84	24.3	1	1	0	0
0.85	0.84	0.86	23.2	0.5	0.5	0.5	0.5
0.98	0.96	1	24	1	1	0	0
1	0.99	1.01	25.8	0.5	0.5	0.5	0.5
1.01	0.99	1.02	24	2	2	20	20
1.04	1.04	1.04	22	2	2	0	0
1.11	1.1	1.12	25.8	0.5	0.5	0.5	0.5
1.13	1.13	1.13	24	5	5	0	0
1.17	1.17	1.17	25.2	0.8	0.8	0	0
1.21	1.19	1.22	25	2	2	20	20
1.22	1.21	1.23	25.3	0.5	0.5	0.5	0.5

Table 1: *continued*

p_{lab} (GeV)	Max. p_{lab} (GeV)	Min. p_{lab} (GeV)	Experimental Cross Section (mb)	Stat. Error Max.	Stat. Error Min.	Systematic Error (+%)	Systematic Error (-%)
1.23	1.23	1.23	24.2	1.6	1.6	0	0
1.28	1.28	1.28	25.1	0.8	0.8	0	0
1.29	1.29	1.29	23	2	2	0	0
1.29	1.29	1.29	24.7	1	1	0	0
1.32	1.31	1.33	24.6	0.5	0.5	0.5	0.5
1.42	1.42	1.43	24.3	0.6	0.6	0.5	0.5
1.46	1.44	1.49	21	2	2	20	20
1.48	1.36	1.59	24	3	3	0	0
1.53	1.52	1.54	24.1	0.5	0.5	0.5	0.5
1.63	1.63	1.63	26	3	3	0	0
1.66	1.66	1.66	26.8	2.3	2.3	0	0
1.66	1.64	1.68	24.8	0.9	0.9	0	0
1.69	1.68	1.7	24.7	0.5	0.5	0.5	0.5
1.69	1.69	1.69	28.2	2.1	2.1	0	0
1.7	1.67	1.72	19	3	3	20	20
1.79	1.77	1.8	22.7	0.5	0.5	0.5	0.5
1.89	1.87	1.9	22.5	0.5	0.5	0.5	0.5
1.99	1.98	2	22.1	0.5	0.5	0.5	0.5
2.2	2.2	2.2	22.2	3.4	3.4	0	0
2.23	2.23	2.23	19.86	0.73	0.64	0	0
2.8	2.8	2.8	16.3	1	1	3.5	3.5
2.81	2.81	2.81	19.21	0.48	0.48	1.5	1.5
3	3	3	17.2	0.7	0.7	4	4
3.04	3.01	3.06	17	3	3	15	15
3.65	3.65	3.65	15.2	0.6	0.6	4	4
3.67	3.64	3.7	15.32	0.76	0.76	0	0
4	3.96	4.04	13.5	0.3	0.3	0	0
4.15	4.1	4.2	11.6	2.6	2.6	0	0
4.8	4.8	4.8	14.4	1.2	1.2	3.5	3.5
5	5	5	12.7	0.5	0.5	4	4
5.26	5.21	5.3	10	2	2	15	15
5.52	5.51	5.53	11.99	0.25	0.25	0	0
5.96	5.96	5.96	10	2.1	2.1	0	0
6	6	6	11.5	0.5	0.5	4	4
6.6	6.59	6.61	11.47	0.33	0.33	0	0
6.8	6.8	6.8	11.79	0.22	0.22	0	0

p_{lab} (GeV)	Max. p_{lab} (GeV)	Min. p_{lab} (GeV)	Experimental Cross Section (mb)	Stat. Error Max.	Stat. Error Min.	Systematic Error (+%)	Systematic Error (-%)
6.8	6.8	6.8	10.6	0.6	0.6	3.5	3.5
6.92	6.85	7	11.4	0.5	0.5	0	0
7.03	6.96	7.09	8	2	2	15	15
7.08	7.08	7.08	9.7	1	1	0	0
7.08	7.08	7.08	9.8	0.9	0.9	0	0
8.1	8	8.2	10.8	0.4	0.4	0	0
8.5	8.5	8.5	8.74	0.4	0.4	0	0
8.8	8.8	8.8	11.71	0.22	0.22	0	0
8.8	8.8	8.8	9.8	0.3	0.3	0	0
8.9	8.9	8.9	10.1	0.5	0.5	3.5	3.5
9	9	9	10.84	0.32	0.32	0	0
9.11	9.1	9.12	10.8	0.8	0.8	0	0
9.39	9.39	9.39	8.6	0.8	0.8	0	0
9.89	9.89	9.89	10	3	3	0	0
9.9	9.8	10	10.2	0.5	0.5	15	15
10.01	10	10.02	10.2	0.6	0.6	0	0
10.8	10.8	10.8	11.04	0.22	0.22	0	0
10.9	10.9	10.9	9.9	0.5	0.5	3.5	3.5
12	12	12	9.87	0.23	0.23	0	0
12	12	12	9.85	0.2	0.2	0	0
12.1	12.1	12.1	10.4	1.7	1.7	0	0
12.8	12.8	12.8	10.89	0.3	0.3	0	0
13.2	13.2	13.2	8.87	0.29	0.29	3.5	3.5
14.8	14.8	14.8	10.48	0.32	0.32	0	0
14.91	14.91	14.91	11	4	4	0	0
15	15	15	8.13	0.3	0.3	0	0
15.1	14.95	15.25	9.7	0.5	0.5	15	15
15.5	15.5	15.5	9.2	1.4	1.4	0	0
15.5	15.5	15.5	8.75	0.29	0.29	3.5	3.5
16.2	16.2	16.2	9.36	0.49	0.49	0	0
16.7	16.7	16.7	9.74	0.37	0.37	0	0
18.6	18.6	18.6	10.2	1.8	1.8	0	0
18.9	18.9	18.9	8.59	0.17	0.17	3.5	3.5
19	19	19	8.7	0.5	0.5	0	0
19.2	19.2	19.2	9.4	1.3	1.3	0	0
19.6	19.6	19.6	9.64	0.44	0.44	0	0

p_{lab} (GeV)	Max. p_{lab} (GeV)	Min. p_{lab} (GeV)	Experimental Cross Section (mb)	Stat. Error Max.	Stat. Error Min.	Systematic Error (+%)	Systematic Error (-%)
20	19.8	20.2	9	0.5	0.5	15	15
21.4	21.4	21.4	8	1.6	1.6	0	0
21.7	21.7	21.7	8.15	0.16	0.16	3.5	3.5
23.5	23.5	23.5	8.3	1.2	0.7	0	0
24	24	24	8.3	0.2	0.2	0	0
24.5	24.5	24.5	8.8	0.3	0.3	0	0
24.6	24.6	24.6	8.02	0.16	0.16	3.5	3.5
26.2	26.2	26.2	9.8	2.2	2.2	0	0
27.5	27.5	27.5	7.96	0.15	0.15	3.5	3.5
29.7	29.4	30	8.2	0.6	0.6	15	15
30	30	30	7.7	0.2	0.2	0	0
30.5	30.5	30.5	7.87	0.14	0.14	3.5	3.5
33.3	33.3	33.3	7.66	0.14	0.14	3.5	3.5
36.2	36.2	36.2	7.7	0.11	0.11	3.5	3.5
38	38	38	7.6	0.1	0.1	3.5	3.5
40.6	40.6	40.6	7.52	0.11	0.11	3.5	3.5
45.2	45.2	45.2	7.4	0.11	0.11	3.5	3.5
50	49.7	50.3	7.61	0.29	0.29	0	0
50	50	50	7	0.2	0.2	0	0
50	50	50	7.56	0.12	0.12	0	0
50.6	50.6	50.6	7.48	0.12	0.12	3.5	3.5
52.1	52.1	52.1	7.33	0.12	0.12	3.5	3.5
54.4	54.4	54.4	7.23	0.11	0.11	3.5	3.5
57	57	57	7.21	0.1	0.1	3.5	3.5
58	58	58	7.49	8.00E-02	8.00E-02	0	0
60	60	60	6.6	0.7	0.7	0	0
60.2	60.2	60.2	7.25	0.1	0.1	3.5	3.5
63.5	63.5	63.5	6.89	9.00E-02	9.00E-02	3.5	3.5
66.1	66.1	66.1	7.07	9.00E-02	9.00E-02	3.5	3.5
69.2	69.2	69.2	6.86	9.00E-02	9.00E-02	3.5	3.5
69.8	69.8	69.8	6.86	0.1	0.1	3.5	3.5
70	69.58	70.42	7.41	0.31	0.31	0	0
70	70	70	7.1	0.2	0.2	0	0

Table 2: Data for Figure 11 [15] at $p_{lab} = 1.18$ GeV.

t(GeV^2)	Experimental Cross Section ($\frac{mb}{GeV^2}$)	Experimental Uncertainty ($\frac{mb}{GeV^2}$)
-0.14	47.97	3.14
-0.17	46.29	3.02
-0.2	46.37	3.02
-0.23	44.01	2.87
-0.26	43.5	3.47
-0.29	41.11	3.28
-0.33	36.93	2.93
-0.36	38.23	3.04
-0.39	37.44	2.99
-0.42	35.14	2.8
-0.45	34.6	2.76
-0.49	34.73	2.77
-0.52	34.92	2.79

Table 3: Data for Figure 12 [15] at $p_{lab} = 1.38$ GeV.

t(GeV^2)	Experimental Cross Section ($\frac{\text{mb}}{\text{GeV}^2}$)	Experimental Uncertainty ($\frac{\text{mb}}{\text{GeV}^2}$)
-0.16	48.59	2.78
-0.2	42.02	2.77
-0.23	38.72	2.55
-0.27	34.35	2.77
-0.31	29.38	1.94
-0.35	27.92	2.26
-0.39	21.35	1.42
-0.44	20.06	1.62
-0.48	19.21	1.56
-0.52	16.37	1.34
-0.56	15.52	1.27
-0.6	14.91	1.22
-0.65	15.52	1.04

Table 4: Data for Figure 13 [15] at $p_{lab} = 2.74$ GeV.

t(GeV^2)	Experimental Cross Section ($\frac{\text{mb}}{\text{GeV}^2}$)	Experimental Uncertainty ($\frac{\text{mb}}{\text{GeV}^2}$)
-0.14	42.05	3.33
-0.23	23.35	1.85
-0.33	15.03	1.22
-0.44	7.28	0.58
-0.58	4.14	0.34
-0.7	2.57	0.79
-0.83	1.52	0.12
-0.97	1.05	0.09
-1.06	1.16	0.13
-1.17	0.91	0.08
-1.31	0.66	0.05
-1.46	0.73	0.06
-1.61	0.67	0.05
-1.76	0.6	0.05

Table 5: Data for Figure 14 [16] at $p_{lab} = 1.399$ GeV.

t(GeV^2)	Experimental Cross Section ($\frac{mb}{GeV^2}$)	Experimental Uncertainty ($\frac{mb}{GeV^2}$)
-0.00538	116.9	3.2
-0.00604	109.1	3.0
-0.00672	113.2	2.9
-0.00744	110.3	2.8
-0.00818	106.9	2.6
-0.00899	108.1	2.6
-0.00985	107.8	2.5
-0.01074	108.2	2.3
-0.01167	112.3	2.4
-0.01263	106.0	2.2
-0.01364	104.2	2.2
-0.01468	103.2	2.2
-0.01576	105.5	2.2
-0.01688	103.0	2.1
-0.01803	107.2	2.2
-0.01923	104.2	2.1
-0.02046	103.5	2.0
-0.02173	104.0	1.9
-0.02303	100.8	1.8
-0.02437	97.5	1.9
-0.02575	100.8	1.8
-0.02717	101.0	1.8
-0.02862	97.5	1.8
-0.03011	96.9	1.8
-0.03163	96.9	1.8

Table 6: Data for Figure 15 [16] at $p_{lab} = 1.457$ GeV.

t(GeV^2)	Experimental Cross Section ($\frac{\text{mb}}{\text{GeV}^2}$)	Experimental Uncertainty ($\frac{\text{mb}}{\text{GeV}^2}$)
-0.00728	119.0	2.5
-0.00806	117.2	2.4
-0.00890	116.2	2.2
-0.00978	113.7	2.3
-0.01071	113.0	1.9
-0.01168	115.8	1.8
-0.01269	114.5	1.8
-0.01374	111.4	1.8
-0.01483	112.7	1.8
-0.01597	112.5	1.7
-0.01714	109.0	1.7
-0.01836	110.2	1.7
-0.01962	111.4	1.7
-0.02091	108.7	1.6
-0.02225	106.2	1.6
-0.02363	103.6	1.6
-0.02505	103.2	1.6
-0.02651	103.8	1.6
-0.02801	100.4	1.6
-0.02955	101.7	1.5
-0.03112	100.1	1.5
-0.03274	98.4	1.5
-0.03440	99.1	1.5

Table 7: Data for Figure 16 [16] at $p_{lab} = 1.629$ GeV.

t(GeV^2)	Experimental Cross Section ($\frac{mb}{GeV^2}$)	Experimental Uncertainty ($\frac{mb}{GeV^2}$)
-0.00641	130.2	2.9
-0.00723	130.0	2.7
-0.00810	126.4	2.6
-0.00902	122.6	3.0
-0.01002	120.0	3.1
-0.01107	115.3	3.0
-0.01217	117.3	3.0
-0.01333	121.0	3.0
-0.01453	121.4	2.9
-0.01579	111.4	2.9
-0.01710	117.9	2.8
-0.01846	113.5	2.8
-0.01987	114.7	2.6
-0.02133	112.5	2.5
-0.02284	108.0	2.5
-0.02440	107.5	2.5
-0.02602	105.5	2.4
-0.02768	103.2	2.4
-0.02939	98.5	2.3
-0.03115	104.5	2.3
-0.03297	97.6	2.2
-0.03483	98.3	2.2
-0.03674	97.6	2.2

Table 8: Data for Figure 17 [16] at $p_{lab} = 1.686$ GeV.

t(GeV^2)	Experimental Cross Section ($\frac{mb}{GeV^2}$)	Experimental Uncertainty ($\frac{mb}{GeV^2}$)
-0.00701	131	3.5
-0.00764	129.6	3.4
-0.00827	129.9	3.4
-0.00890	127.5	3.4
-0.00953	124.1	3.3
-0.01016	128.3	3.4
-0.01079	124.3	3.3
-0.01142	123.8	3.2
-0.01205	122.5	3.3
-0.01268	126.2	3.4
-0.01331	115.1	3.2
-0.01394	120.8	3.3
-0.01457	112.9	3.2
-0.01520	119.2	3.3
-0.01583	117.9	3.3
-0.01646	115.3	3.2
-0.01709	121.2	3.3
-0.01772	116.5	3.2
-0.01835	117.5	3.3
-0.01987	115.8	2.4
-0.02024	114.7	2.3
-0.02150	109.1	2.1
-0.02276	114	2.3
-0.02402	112.8	2.2
-0.02528	110.6	2.1
-0.02682	107.3	1.7
-0.02925	104.2	1.7
-0.03169	103	1.7
-0.03412	103.3	1.7
-0.03656	96.9	1.6
-0.03900	105.1	1.7
-0.04143	97.2	1.6
-0.04387	98.5	1.6
-0.04630	99.7	1.7
-0.04874	92.9	1.6
-0.05118	91	1.6
-0.05361	95	1.6

Table 8: *continued*

t(GeV^2)	Experimental Cross Section ($\frac{\text{mb}}{\text{GeV}^2}$)	Experimental Uncertainty ($\frac{\text{mb}}{\text{GeV}^2}$)
-0.05605	97.1	1.6
-0.05848	93.4	1.6
-0.06092	93.2	1.6
-0.06336	88.4	1.6
-0.06579	86.4	1.6
-0.06823	85.3	1.6
-0.07066	90.1	1.6
-0.07310	83.6	1.4
-0.07554	86.5	1.6
-0.00603	135.3	3
-0.00686	128.6	2.9
-0.00773	132.7	2.7
-0.00866	126.6	2.7
-0.00966	124.2	2.5
-0.01072	122.7	2.6
-0.01184	122.8	2.6
-0.01302	116.8	2.4
-0.01425	115.1	2.3
-0.01554	112.9	2.3
-0.01689	113.6	2.3
-0.01828	116.9	2.3
-0.01974	112	2.3
-0.02125	109.1	2.2
-0.02281	110.7	2.3
-0.02442	106.3	2.1
-0.02609	105.9	2.1
-0.02782	107.2	2.1
-0.02960	104.3	2
-0.03143	100.2	2
-0.03331	102.6	2
-0.03525	97.5	1.9
-0.03724	97.6	1.9
-0.03929	97.1	1.9

Table 9: Data for Figure 18 [17] at $p_{lab} = 1.896$ GeV.

t(GeV^2)	Experimental Cross Section ($\frac{\mu b}{GeV^2}$)	Experimental Uncertainty ($\frac{\mu b}{GeV^2}$)
-0.475	6900	1020
-0.525	7070	511
-0.575	4740	273
-0.625	4510	233
-0.675	3650	196
-0.725	3070	168
-0.775	3100	168
-0.825	2500	148
-0.875	2460	141
-0.925	2210	126
-0.975	2100	114
-1.025	2190	115
-1.075	1930	108

Table 10: Data for Figure 19 [17] at $p_{lab} = 2.015$ GeV.

t(GeV^2)	Experimental Cross Section ($\frac{\mu b}{GeV^2}$)	Experimental Uncertainty ($\frac{\mu b}{GeV^2}$)
-0.525	4160	822
-0.575	4400	354
-0.625	4280	223
-0.675	4170	187
-0.725	3340	145
-0.775	2860	124
-0.825	2750	116
-0.875	2260	101
-0.925	2140	96.3
-0.975	2200	92.2
-1.025	2070	85.4
-1.075	2020	78.3
-1.125	1970	75.6
-1.175	1960	76.8

Table 11: Data for Figure 20 [17] at $p_{lab} = 2.139$ GeV.

t(GeV^2)	Experimental Cross Section ($\frac{\mu b}{GeV^2}$)	Experimental Uncertainty ($\frac{\mu b}{GeV^2}$)
-0.475	6900	1020
-0.575	1020	309
-0.625	2290	185
-0.675	2960	152
-0.725	2460	114
-0.775	2550	108
-0.825	2110	88.1
-0.875	2340	91.3
-0.925	1940	77.9
-0.975	1830	72.8
-1.025	1670	67.1
-1.075	1530	61.4
-1.125	1440	55.9
-1.175	1480	55.9
-1.225	1390	53.5
-1.275	1380	53.7

Table 12: Data for Figure 21 [17] at $p_{lab} = 2.508$ GeV.

t(GeV^2)	Experimental Cross Section ($\frac{\mu b}{GeV^2}$)	Experimental Uncertainty ($\frac{\mu b}{GeV^2}$)
-0.725	166	174
-0.775	1050	185
-0.825	1860	165
-0.875	1520	103
-0.925	1510	88.6
-0.975	1450	78.9
-1.025	1230	66
-1.075	1260	67.8
-1.125	1220	64.9
-1.175	1080	56.7
-1.225	1050	54.8
-1.275	869	46.3
-1.325	936	45.6
-1.375	898	41.3
-1.425	923	40.9
-1.475	871	37.7
-1.525	851	36.5
-1.575	852	36.5

Table 13: Data for Figure 22 [17] at $p_{lab} = 3.410$ GeV.

t(GeV^2)	Experimental Cross Section ($\frac{\mu b}{GeV^2}$)	Experimental Uncertainty ($\frac{\mu b}{GeV^2}$)
-1.325	2.61	156
-1.375	96.3	61
-1.425	137	44.9
-1.475	133	29.1
-1.525	264	33.9
-1.575	273	26.4
-1.625	234	21.8
-1.675	228	18.9
-1.725	215	17.7
-1.775	215	16.5
-1.825	194	14.2
-1.875	190	13.9
-1.925	240	15.1
-1.975	195	13.2
-2.025	181	12.3
-2.075	186	12.2
-2.125	166	11.2
-2.175	175	11.4
-2.225	159	10.4
-2.275	172	10.8
-2.325	146	9.99
-2.375	150	10

Table 14: Data for Figure 23 [17] at $p_{lab} = 5.055$ GeV.

t(GeV^2)	Experimental Cross Section ($\frac{\mu b}{GeV^2}$)	Experimental Uncertainty ($\frac{\mu b}{GeV^2}$)
-2.05	11.2	8.3
-2.15	15.4	7.57
-2.25	6.51	3.76
-2.35	19.5	4.66
-2.45	24	4.32
-2.55	16.2	3.11
-2.65	18.1	3.03
-2.75	15.6	2.49
-2.85	17.4	2.63
-2.95	14.1	2.29
-3.05	14.8	2.15
-3.15	13.3	2.11
-3.25	16.9	2.39
-3.35	13	2.06
-3.45	17	2.32
-3.55	11.6	1.89
-3.65	13.9	2.1
-3.75	11.4	1.8
-3.85	7.25	1.44

Table 15: Data for Figure 24 [17] at $p_{lab} = 6.57$ GeV.

t(GeV^2)	Experimental Cross Section ($\frac{\mu b}{GeV^2}$)	Experimental Uncertainty ($\frac{\mu b}{GeV^2}$)
-2.85	4.1	3.29
-2.95	8.46	3.15
-3.05	3.88	0.94
-3.15	4.04	0.79
-3.25	3.5	0.64
-3.35	4.3	0.64
-3.45	3.65	0.57
-3.55	4.34	0.57
-3.65	2.44	0.38
-3.75	2.82	0.38
-3.85	2.63	0.34
-3.95	2.02	0.3
-4.05	2.04	0.29
-4.15	1.68	0.25
-4.25	1.73	0.24
-4.35	1.64	0.23
-4.45	1.86	0.25
-4.55	1.51	0.22
-4.65	1.96	0.25
-4.75	1.61	0.22
-4.85	1.45	0.21
-4.95	1.56	0.21
-5.05	1.7	0.22
-5.15	1.09	0.17
-5.25	1.39	0.2

Table 16: Data for Figure 25 [17] at $p_{lab} = 8.022$ GeV.

t(GeV^2)	Experimental Cross Section ($\frac{\mu b}{GeV^2}$)	Experimental Uncertainty ($\frac{\mu b}{GeV^2}$)
-4.25	0.565	0.2380
-4.35	0.360	0.1890
-4.45	0.392	0.1750
-4.55	0.850	0.2240
-4.65	0.622	0.1950
-4.75	0.363	0.1380
-4.85	0.291	0.1110
-4.95	0.373	0.1210
-5.05	0.299	0.1030
-5.15	0.430	0.1170
-5.25	0.204	0.0819
-5.35	0.0958	0.0584
-5.45	0.483	0.1150
-5.55	0.163	0.0644
-5.65	0.316	0.0873
-5.75	0.284	0.0815

Table 17: Data for Figure 26 [18] at $p_{lab} = 3.00$ GeV.

t(GeV^2)	Experimental Cross Section ($\frac{\text{mb}}{\text{GeV}^2}$)	Experimental Uncertainty ($\frac{\text{mb}}{\text{GeV}^2}$)
0.000	109.6	3.5
-0.025	98.9	3.9
-0.035	93.2	4.2
-0.045	81.9	2.5
-0.055	77.7	2.3
-0.065	71.5	2.2
-0.075	67.5	2.1
-0.085	58.3	1.9
-0.095	58.1	1.9
-0.110	49.5	1.3
-0.130	45.1	1.2
-0.150	39.8	1.1
-0.170	34.5	1.1
-0.190	28.52	0.96
-0.210	23.89	0.88
-0.230	21.91	0.84
-0.250	20.67	0.82
-0.270	17.73	0.76
-0.290	15.16	0.7
-0.310	13.68	0.67
-0.330	11.76	0.63
-0.350	9.73	0.57
-0.370	9.61	0.57
-0.390	7.87	0.52
-0.420	7.15	0.36
-0.460	5.58	0.32
-0.500	4.93	0.3
-0.540	3.7	0.27
-0.580	2.99	0.25
-0.650	2.34	0.15
-0.750	1.52	0.13
-0.850	0.99	0.11
-0.950	0.77	0.11
-1.050	0.64	0.12
-1.150	0.82	0.17
-1.250	0.38	0.12
-1.350	0.42	0.13

Table 17: *continued*

t(GeV^2)	Experimental Cross Section ($\frac{\text{mb}}{\text{GeV}^2}$)	Experimental Uncertainty ($\frac{\text{mb}}{\text{GeV}^2}$)
-1.450	0.5	0.21

Table 18: Data for Figure 27 [18] at $p_{lab} = 3.65$ GeV.

t(GeV^2)	Experimental Cross Section ($\frac{\text{mb}}{\text{GeV}^2}$)	Experimental Uncertainty ($\frac{\text{mb}}{\text{GeV}^2}$)
0.000	103.4	3.6
-0.035	80.9	3.8
-0.045	71.9	2.6
-0.055	70.4	2.3
-0.065	63	2.2
-0.075	59.6	2.2
-0.085	55	2
-0.095	51.4	1.9
-0.11	45.1	1.3
-0.13	40.7	1.2
-0.15	33.6	1.1
-0.17	30.1	1
-0.19	25.26	0.99
-0.21	23.19	0.95
-0.23	19.62	0.87
-0.25	18.24	0.84
-0.27	15.66	0.78
-0.29	11.84	0.68
-0.31	10.29	0.64
-0.33	8.86	0.59
-0.35	9.13	0.6
-0.37	6.91	0.52
-0.39	6.59	0.51
-0.42	5.63	0.34
-0.46	4.83	0.32
-0.5	3.9	0.29
-0.54	3.05	0.26
-0.58	2.54	0.23
-0.65	1.85	0.13
-0.75	1.09	0.1
-0.85	0.95	0.1
-0.95	0.69	0.09
-1.05	0.65	0.1
-1.15	0.43	0.08
-1.25	0.4	0.08
-1.35	0.26	0.07
-1.45	0.28	0.08

Table 18: *continued*

t(GeV^2)	Experimental Cross Section ($\frac{\text{mb}}{\text{GeV}^2}$)	Experimental Uncertainty ($\frac{\text{mb}}{\text{GeV}^2}$)
-1.55	0.16	0.07
-1.65	0.09	0.05
-1.75	0.14	0.08

Table 19: Data for Figure 28 [18] at $p_{lab} = 5.00$ GeV.

t(GeV^2)	Experimental Cross Section ($\frac{\text{mb}}{\text{GeV}^2}$)	Experimental Uncertainty ($\frac{\text{mb}}{\text{GeV}^2}$)
0.000	96.3	3.4
-0.035	73.1	2.6
-0.045	68.3	2.1
-0.055	62.1	1.8
-0.065	56.7	1.8
-0.075	51.3	1.7
-0.085	48.5	1.6
-0.095	42.4	1.5
-0.11	38.2	1
-0.13	34.8	0.99
-0.15	30.15	0.92
-0.17	25.17	0.84
-0.19	22.78	0.8
-0.21	17.48	0.7
-0.23	16.82	0.69
-0.25	13.4	0.61
-0.27	12.06	0.58
-0.29	10.47	0.54
-0.31	8.55	0.49
-0.33	8.05	0.48
-0.35	6.75	0.44
-0.37	6.47	0.43
-0.39	5.54	0.4
-0.42	4.19	0.24
-0.46	3.64	0.23
-0.5	2.64	0.19
-0.54	2.15	0.18
-0.58	1.66	0.16
-0.65	1.227	0.089
-0.75	0.687	0.068
-0.85	0.598	0.065
-0.95	0.337	0.049
-1.05	0.226	0.041
-1.15	0.197	0.039
-1.25	0.234	0.043
-1.35	0.131	0.033
-1.45	0.125	0.033

Table 19: *continued*

t(GeV^2)	Experimental Cross Section ($\frac{\text{mb}}{\text{GeV}^2}$)	Experimental Uncertainty ($\frac{\text{mb}}{\text{GeV}^2}$)
-1.55	0.052	0.021
-1.65	0.055	0.023
-1.75	0.059	0.025
-1.85	0.043	0.021
-1.95	0.046	0.022

Table 20: Data for Figure 29 [18] at $p_{lab} = 6.00$ GeV.

t(GeV^2)	Experimental Cross Section ($\frac{mb}{GeV^2}$)	Experimental Uncertainty ($\frac{mb}{GeV^2}$)
0.000	93.6	3.3
-0.045	62.8	1.9
-0.055	61.4	1.7
-0.065	52.7	1.6
-0.075	46.2	1.5
-0.085	42.3	1.4
-0.095	38.9	1.4
-0.11	35.57	0.95
-0.13	31.56	0.89
-0.15	27.25	0.83
-0.17	21.74	0.74
-0.19	20.11	0.71
-0.21	17.38	0.66
-0.23	14.61	0.61
-0.25	12.9	0.57
-0.27	10.43	0.51
-0.29	9.34	0.49
-0.31	7.44	0.43
-0.33	6.14	0.39
-0.35	5.79	0.38
-0.37	5.09	0.36
-0.39	4.91	0.35
-0.42	4.05	0.23
-0.46	2.7	0.19
-0.5	2.37	0.17
-0.54	1.77	0.15
-0.58	1.35	0.13
-0.65	0.982	0.076
-0.75	0.579	0.059
-0.85	0.321	0.045
-0.95	0.262	0.041
-1.05	0.134	0.029
-1.15	0.146	0.031
-1.25	0.065	0.021
-1.35	0.074	0.022
-1.45	0.064	0.021
-1.55	0.058	0.020

Table 20: *continued*

t(GeV^2)	Experimental Cross Section ($\frac{\text{mb}}{\text{GeV}^2}$)	Experimental Uncertainty ($\frac{\text{mb}}{\text{GeV}^2}$)
-1.65	0.048	0.019
-1.75	0.035	0.016
-1.85	0.022	0.012

Table 21: Data for Figure 30 [19] at $p_{lab} = 9.0$ GeV.

t(GeV^2)	Uncertainty t (GeV^2)	Experimental Cross Section ($\frac{\text{mb}}{\text{GeV}^2}$)	Experimental Uncertainty ($\frac{\text{mb}}{\text{GeV}^2}$)
-0.71	0.02	290	15
-0.73	0.02	286	15
-0.75	0.02	234	12
-0.77	0.02	249	13
-0.79	0.02	202	11
-0.81	0.02	214	12
-0.83	0.02	182	10
-0.85	0.02	156	9.4
-0.87	0.02	138	8.7
-0.89	0.02	121	7.7
-0.91	0.02	107	7.1
-0.93	0.02	113	7.6
-0.95	0.02	90.3	6.5
-0.97	0.02	80.5	5.9
-0.99	0.02	78.4	6
-1.01	0.02	69.8	5.6
-1.03	0.02	64.5	5.2
-1.05	0.02	58	5.1
-1.07	0.02	41.8	4
-1.09	0.02	39.8	4
-1.15	0.1	35	1.7
-1.25	0.1	22.9	1.4
-1.35	0.1	17.7	1.3
-1.45	0.1	12.6	1
-1.55	0.1	9.69	0.94
-1.65	0.1	12.17	1.14
-1.75	0.1	8.59	0.93
-1.85	0.1	6.7	0.77
-1.95	0.1	5.93	0.76
-2.1	0.2	4.17	0.42
-2.3	0.2	3.11	0.37
-2.5	0.2	3.09	0.41
-2.75	0.3	2.26	0.28
-3.05	0.3	1.27	0.23
-3.35	0.3	1.18	0.27
-3.65	0.3	1.19	0.26
-4	0.4	0.44	0.15

Table 21: *continued*

t(GeV^2)	Uncertainty t (GeV^2)	Experimental Cross Section ($\frac{\text{mb}}{\text{GeV}^2}$)	Experimental Uncertainty ($\frac{\text{mb}}{\text{GeV}^2}$)
-4.4	0.4	0.32	0.1
-4.8	0.4	0.17	0.1

Table 22: Data for Figure 31 [20] at $p_{lab} = 10.4$ GeV. Note that 1.0E+01 is defined as 1.0×10^1.

t(GeV^2)	Experimental Cross Section ($\frac{\text{mb}}{\text{GeV}^2}$)	Experimental Uncertainty ($\frac{\text{mb}}{\text{GeV}^2}$)
-0.025	7.514E+01	5.140E-01
-0.035	6.688E+01	4.752E-01
-0.045	6.184E+01	4.443E-01
-0.055	5.660E+01	4.174E-01
-0.065	5.167E+01	3.907E-01
-0.075	4.788E+01	3.761E-01
-0.085	4.334E+01	3.578E-01
-0.095	3.973E+01	3.463E-01
-0.105	3.721E+01	3.295E-01
-0.115	3.354E+01	3.148E-01
-0.125	3.123E+01	3.001E-01
-0.135	2.884E+01	2.872E-01
-0.145	2.677E+01	2.801E-01
-0.155	2.412E+01	2.589E-01
-0.165	2.185E+01	2.494E-01
-0.175	1.996E+01	2.397E-01
-0.185	1.873E+01	2.294E-01
-0.195	1.759E+01	2.239E-01
-0.205	1.581E+01	2.116E-01
-0.215	1.492E+01	2.060E-01
-0.225	1.412E+01	1.979E-01
-0.235	1.270E+01	1.869E-01
-0.245	1.168E+01	1.826E-01
-0.255	1.065E+01	1.751E-01
-0.265	9.933E+00	1.693E-01
-0.275	9.283E+00	1.666E-01
-0.285	8.343E+00	1.615E-01
-0.295	8.150E+00	1.630E-01
-0.305	7.522E+00	1.576E-01
-0.315	6.884E+00	1.528E-01
-0.325	6.526E+00	1.515E-01
-0.335	5.686E+00	1.489E-01
-0.345	5.598E+00	1.463E-01
-0.355	5.150E+00	1.431E-01
-0.365	4.993E+00	1.427E-01
-0.375	4.339E+00	1.341E-01

Table 22: *continued*

t(GeV^2)	Experimental Cross Section ($\frac{\text{mb}}{\text{GeV}^2}$)	Experimental Uncertainty ($\frac{\text{mb}}{\text{GeV}^2}$)
-0.385	4.214E+00	1.362E-01
-0.395	3.597E+00	1.275E-01
-0.410	3.011E+00	8.478E-02
-0.430	2.798E+00	8.154E-02
-0.450	2.355E+00	7.958E-02
-0.470	2.113E+00	7.694E-02
-0.490	1.672E+00	6.929E-02
-0.510	1.822E+00	7.162E-02
-0.530	1.328E+00	6.208E-02
-0.550	1.142E+00	5.769E-02
-0.570	8.937E-01	5.334E-02
-0.590	7.854E-01	4.874E-02
-0.625	6.785E-01	2.949E-02
-0.675	4.553E-01	2.495E-02
-0.725	3.598E-01	2.245E-02
-0.775	2.075E-01	1.695E-02
-0.825	1.602E-01	1.549E-02
-0.875	1.154E-01	1.298E-02
-0.925	5.571E-02	1.051E-02
-0.975	4.856E-02	9.548E-03
-1.050	3.252E-02	6.097E-03
-1.150	1.944E-02	4.355E-03
-1.250	2.592E-02	6.062E-03
-1.350	2.032E-02	6.458E-03
-1.450	1.539E-02	5.617E-03

Table 23: Data for Figure 32 [21] at $p_{lab} = 9.43$ GeV.

t(GeV^2)	Experimental Cross Section ($\frac{\text{mb}}{\text{GeV}^2}$)	Experimental Uncertainty ($\frac{\text{mb}}{\text{GeV}^2}$)
-0.00079	611.34	14.49
-0.00095	491.5	12.67
-0.00112	390	6.3
-0.00130	304.58	7.21
-0.00150	272.56	3.89
-0.00171	230.66	6.67
-0.00172	245.54	5.85
-0.00194	206.38	3.58
-0.00218	188.17	4.27
-0.00244	164.52	2.98
-0.00271	160.36	4.41
-0.00299	149.16	2.72
-0.00329	146.02	3.81
-0.00360	135.4	3.37
-0.00361	136.46	2.81
-0.00393	128.64	3.14
-0.00426	128.67	3.42
-0.00462	117.64	3.34
-0.00499	114.14	2.81
-0.00537	113.97	2.54
-0.00576	109.31	1.69
-0.00618	105.82	2.42
-0.00660	107.52	2.32
-0.00704	105.54	2.6
-0.00749	104.55	2.67
-0.00796	100.65	2.26
-0.00846	99.64	2.1
-0.00895	97.45	1.41
-0.00947	95.99	2
-0.00999	96.24	1.94
-0.01052	94.15	2.2
-0.01108	91.37	2.2
-0.01165	90.53	1.92
-0.01283	88.66	1.61

Table 24: Data for Figure 33 [21] at $p_{lab} = 13.16$ GeV.

t(GeV^2)	Experimental Cross Section ($\frac{mb}{GeV^2}$)	Experimental Uncertainty ($\frac{mb}{GeV^2}$)
-0.00920	86.18	1.04
-0.01141	83.7	1.8
-0.01358	82.34	1.8
-0.01541	80.29	1.04
-0.01718	79.67	1.8
-0.01914	75.85	1.16
-0.02759	65.9	1.8
-0.03004	66.62	1.8
-0.04509	55.59	1.8
-0.04702	50.34	1.8
-0.04898	52.55	1.27
-0.05139	51.72	1.8
-0.05468	53.57	1.8
-0.06606	42.88	1.8
-0.06837	42.04	1.8
-0.07071	44.43	1.27
-0.07357	39.26	1.8
-0.07747	40.33	1.8
-0.07865	36.81	0.68
-0.09634	31.92	1.27
-0.09964	31.19	1.8
-0.10412	29.2	1.8

Table 25: Data for Figure 34 [21] at $p_{lab} = 15.52$ GeV.

t(GeV^2)	Experimental Cross Section ($\frac{mb}{GeV^2}$)	Experimental Uncertainty ($\frac{mb}{GeV^2}$)
-0.00890	85.6	1.01
-0.01109	83.44	1.01
-0.01644	77.63	0.9
-0.01906	75.71	1.17
-0.02663	69.8	2.02
-0.02859	64.21	1.43
-0.03053	66.12	1.43
-0.03635	58.57	0.76
-0.04632	54.73	2.02
-0.04830	54.21	2.02
-0.05032	51.44	1.43
-0.05303	50.3	1.43
-0.05617	46.81	2.02
-0.06739	45.02	1.43
-0.06925	42.73	2.02
-0.07116	41.33	1.17
-0.07263	39.91	1.43
-0.07557	40.04	2.02
-0.07600	40.14	2.02
-0.07963	38.21	0.7
-0.08078	36.39	0.76
-0.09487	30.5	2.02
-0.09713	30.81	1.17
-0.09894	29.41	1.43
-0.10249	29.08	1.43
-0.10512	28.32	2.02
-0.10692	29.68	2.02

Table 26: Data for Figure 35 [21] at $p_{lab} = 19.23$ GeV.

t(GeV^2)	Experimental Cross Section ($\frac{\text{mb}}{\text{GeV}^2}$)	Experimental Uncertainty ($\frac{\text{mb}}{\text{GeV}^2}$)
-0.00106	365.07	4.36
-0.00125	302.48	5.53
-0.00146	244.08	4.7
-0.00168	209.18	2.68
-0.00191	192.49	4.55
-0.00192	185.92	2.77
-0.00217	159.26	3.22
-0.00244	142.13	3.01
-0.00272	145.23	2.13
-0.00302	127.57	2.84
-0.00334	121.77	1.96
-0.00366	114.03	1.72
-0.00367	120.17	2.26
-0.00401	106.1	3.31
-0.00402	110.77	1.88
-0.00437	108.16	5.19
-0.00475	103.23	2.31
-0.00514	101.42	2.11
-0.00555	98.58	2.09
-0.00597	93.79	1.34
-0.00642	93.34	0.99
-0.00687	94.82	2.65
-0.00734	89.1	3.82
-0.00782	86.82	1.85
-0.00833	87.55	1.73
-0.00885	84.14	1.71
-0.00940	86.86	1.15
-0.00994	82.92	0.84
-0.01052	82.53	2.23
-0.01110	78.41	3.49
-0.01169	78.93	1.64
-0.01231	78.08	1.51
-0.01294	79.83	1.52
-0.01359	77.8	1.29
-0.01426	77.15	1.11

Table 27: Data for Figure 36 [21] at $p_{lab} = 24.56$ GeV.

t(GeV^2)	Experimental Cross Section ($\frac{\text{mb}}{\text{GeV}^2}$)	Experimental Uncertainty ($\frac{\text{mb}}{\text{GeV}^2}$)
-0.01085	78.87	1.06
-0.01515	75.32	0.82
-0.01691	73.9	0.82
-0.02042	68.61	1.06
-0.02759	63.66	0.75
-0.02948	62.46	1.29
-0.03099	62.76	1.29
-0.03215	57.95	1.83
-0.03781	57.07	0.4
-0.04891	48.45	1.29
-0.05030	47.2	1.83
-0.05230	48.55	0.75
-0.05523	47.59	1.06
-0.05847	45.48	1.29
-0.07044	40.02	1.29
-0.07267	38.37	1.06
-0.07547	37.39	0.75
-0.07921	37.27	1.29
-0.08341	34.45	0.6
-0.08410	32.61	0.69
-0.09696	27.35	1.29
-0.09886	28.66	1.06
-0.10009	28.64	1.83
-0.10277	28.94	0.75
-0.10678	27.58	1.06
-0.11089	25.29	1.06

Table 28: Data for Figure 37 [21] at $p_{lab} = 27.53$ GeV.

t(GeV^2)	Experimental Cross Section ($\frac{\text{mb}}{\text{GeV}^2}$)	Experimental Uncertainty ($\frac{\text{mb}}{\text{GeV}^2}$)
-0.00929	81.53	0.66
-0.01094	77.86	1.15
-0.01234	77.22	1.15
-0.01524	74.4	0.81
-0.01705	71.7	0.81
-0.01877	72.18	1.15
-0.02059	68.29	1.15
-0.02972	60.63	1.41
-0.03126	59.75	1.41
-0.03240	61.35	1.99
-0.03812	56.53	0.44
-0.04861	46.7	1.99
-0.05054	44.84	1.41
-0.05273	46.44	0.81
-0.05532	46.38	1.41
-0.05640	46.63	1.99
-0.05894	46.14	1.41
-0.07134	37.38	1.15
-0.07326	36.77	1.15
-0.07581	37.85	1.41
-0.07622	35.58	1
-0.07917	36.08	1.41
-0.08043	35.56	1.99
-0.08319	34.33	1.15
-0.08461	33.71	0.53
-0.09773	27.49	1.41
-0.09934	28.56	1.41
-0.10060	27.72	1.41
-0.10360	27.83	0.81
-0.10716	28.03	1.41
-0.10859	24.98	1.99
-0.11120	26.77	1.99
-0.11207	24.37	1.41

Table 29: Data for Figure 38 [21] at $p_{lab} = 30.45$ GeV.

t(GeV^2)	Experimental Cross Section ($\frac{\text{mb}}{\text{GeV}^2}$)	Experimental Uncertainty ($\frac{\text{mb}}{\text{GeV}^2}$)
-0.01101	77.01	0.82
-0.01889	69.98	0.82
-0.02787	60.05	0.82
-0.02883	61.12	0.64
-0.03075	57.81	1.43
-0.03239	59.44	1.01
-0.03837	55.61	0.31
-0.04927	48.32	1.01
-0.05069	47.65	0.82
-0.05307	47.41	0.58
-0.05567	45.1	1.01
-0.05678	46.53	1.43
-0.05911	45.87	0.82
-0.07146	38.97	1.01
-0.07319	36.88	0.82
-0.07411	40.03	1.43
-0.07657	37.1	0.58
-0.07966	35.32	1.01
-0.08097	32.49	1.43
-0.08373	33.5	0.82
-0.08515	33.42	0.38
-0.09873	27.26	0.82
-0.10098	27.83	0.82
-0.10396	26.86	1.01
-0.10441	27.37	0.79
-0.10783	25.56	1.01
-0.10931	23.35	1.43
-0.11193	24.18	1.43
-0.11277	24.39	1.01

Table 30: Data for Figure 39 [22] at $p_{lab} = 9.900$ GeV.

t(GeV^2)	Experimental Cross Section ($\frac{\text{mb}}{\text{GeV}^2}$)	Experimental Uncertainty ($\frac{\text{mb}}{\text{GeV}^2}$)
0.000	90.5	0
-0.016	77.1	3.1
-0.022	71.9	2.9
-0.028	68.6	2.7
-0.035	68.8	2.8
-0.043	65.1	2.6
-0.052	58.7	2.3
-0.061	54	2.2
-0.071	49.1	2
-0.082	45.7	1.8
-0.093	39.2	1.6
-0.105	35.2	1.4
-0.118	31.5	1.3
-0.131	28.1	1.2
-0.146	24.1	1
-0.161	21.3	0.9
-0.215	13.9	0.6
-0.234	12.3	0.5
-0.253	10.4	0.5
-0.273	8.1	0.3
-0.316	5.3	0.2
-0.339	4.6	0.19
-0.362	3.94	0.16
-0.385	3.15	0.13
-0.905	0.0830	0.0060
-0.941	0.0750	0.0050
-0.977	0.0620	0.0040
-1.013	0.0490	0.0040
-1.051	0.0407	0.0028
-2.250	0.00355	0.00032
-2.352	0.00293	0.00027
-5.078	0.000191	0.000019

Table 31: Data for Figure 40 [22] at $p_{lab} = 15.100$ GeV. Note that 1.0E+01 is defined as 1.0×10^1.

t(GeV^2)	Experimental Cross Section ($\frac{mb}{GeV^2}$)	Experimental Uncertainty ($\frac{mb}{GeV^2}$)
0.000	84.2	0
-0.027	71.4	3
-0.038	62.5	2.6
-0.051	52.2	2.2
-0.066	47.1	2
-0.082	43.5	1.8
-0.100	36.7	1.5
-0.120	30.3	1.2
-0.141	24.5	1
-0.165	20	0.8
-0.190	16.4	0.7
-0.217	13	0.6
-0.275	6.7	0.28
-0.307	5.48	0.23
-0.341	4.6	0.19
-0.376	3.91	0.16
-0.452	1.87	0.08
-0.492	1.35	0.06
-0.534	0.98	0.04
-0.578	0.69	0.03
-0.623	0.449	0.019
-0.683	0.265	0.013
-0.732	0.177	0.010
-0.783	0.121	0.007
-0.834	0.086	0.006
-0.888	0.059	0.004
-2.055	2.54E-003	1.50E-004
-2.134	2.21E-003	1.30E-004
-2.214	2.08E-003	1.30E-004
-2.294	1.75E-003	1.10E-004
-2.376	1.53E-003	1.10E-004
-4.708	4.35E-005	1.03E-005
-4.914	2.96E-005	9.00E-006

Table 32: Data for Figure 41 [22] at $p_{lab} = 20.000$ GeV. Note that 1.0E+01 is defined as 1.0×10^1.

t(GeV^2)	Experimental Cross Section ($\frac{\text{mb}}{\text{GeV}^2}$)	Experimental Uncertainty ($\frac{\text{mb}}{\text{GeV}^2}$)
0.000	80.7	0
-0.032	62.6	2.5
-0.048	54.1	2.2
-0.067	43.4	1.7
-0.090	34.5	1.4
-0.115	27.8	1.1
-0.144	21.6	0.9
-0.176	16.5	0.7
-0.211	12.2	0.5
-0.249	8.61	0.34
-0.290	6.09	0.24
-0.334	4.18	0.17
-0.381	2.83	0.11
-0.433	1.78	0.07
-0.486	1.1	0.05
-0.542	0.658	0.028
-0.601	0.453	0.020
-0.664	0.258	0.013
-0.732	0.145	0.006
-0.800	0.085	0.004
-0.871	0.0436	0.0017
-0.945	0.0252	0.0010
-1.022	0.0145	0.0010
-1.102	6.87E-003	7.30E-004
-1.203	6.41E-003	4.60E-004
-1.287	4.72E-003	3.90E-004
-1.375	4.07E-003	3.30E-004
-1.464	3.60E-003	3.10E-004
-1.557	3.41E-003	3.00E-004
-3.580	8.30E-005	2.50E-005
-3.847	6.30E-005	1.90E-005

Table 33: Data for Figure 42 [22] at $p_{lab} = 29.700$ GeV. Note that 1.0E+01 is defined as 1.0×10^1.

t(GeV^2)	Experimental Cross Section ($\frac{\text{mb}}{\text{GeV}^2}$)	Experimental Uncertainty ($\frac{\text{mb}}{\text{GeV}^2}$)
0.000	71	0
-0.079	37.4	1.9
-0.097	30.6	1.6
-0.116	25	1.2
-0.137	19.5	1
-0.160	15.3	0.8
-0.184	12.2	0.6
-0.211	9.5	0.4
-0.238	7.8	0.4
-0.268	6.1	0.3
-0.299	4.8	0.3
-0.333	3.44	0.18
-0.367	2.66	0.13
-0.382	2.28	0.12
-0.458	1.18	0.06
-0.541	0.57	0.03
-0.630	0.257	0.013
-0.726	0.113	0.005
-0.834	0.040	0.002
-0.943	0.0138	0.0014
-1.060	5.50E-003	9.00E-004
-1.181	3.20E-003	6.00E-004
-1.320	1.66E-003	2.90E-004
-1.450	2.23E-003	3.30E-004
-1.590	1.68E-003	2.90E-004
-1.740	1.14E-003	1.20E-004
-1.890	8.40E-004	1.20E-004
-2.050	8.20E-004	1.10E-004
-2.210	5.90E-004	9.00E-005
-2.780	3.60E-004	1.60E-004

1. REPORT DATE *(DD-MM-YYYY)*	2. REPORT TYPE	3. DATES COVERED *(From - To)*
01- 02 - 2009	Technical Publication	

4. TITLE AND SUBTITLE	5a. CONTRACT NUMBER
Differential Cross Sections for Proton-Proton Elastic Scattering	
	5b. GRANT NUMBER
	5c. PROGRAM ELEMENT NUMBER

6. AUTHOR(S)	5d. PROJECT NUMBER
Norman, Ryan B.; Dick, Frank; Norbury, John W.; Blattnig, Steve R.	
	5e. TASK NUMBER
	5f. WORK UNIT NUMBER
	651549.02.07.01

7. PERFORMING ORGANIZATION NAME(S) AND ADDRESS(ES)	8. PERFORMING ORGANIZATION REPORT NUMBER
NASA Langley Research Center Hampton, VA 23681-2199	L-19507

9. SPONSORING/MONITORING AGENCY NAME(S) AND ADDRESS(ES)	10. SPONSOR/MONITOR'S ACRONYM(S)
National Aeronautics and Space Administration Washington, DC 20546-0001	NASA
	11. SPONSOR/MONITOR'S REPORT NUMBER(S)
	NASA/TP-2009-215565

12. DISTRIBUTION/AVAILABILITY STATEMENT
Unclassified - Unlimited Subject Category 93 Availability: NASA CASI (443) 757-5802

13. SUPPLEMENTARY NOTES

14. ABSTRACT

Proton-proton elastic scattering is investigated within the framework of the one pion exchange model in an attempt to model nucleon-nucleon interactions spanning the large range of energies important to cosmic ray shielding. A quantum field theoretic calculation is used to compute both differential and total cross sections. A scalar theory is then presented and compared to the one pion exchange model. The theoretical cross sections are compared to proton-proton scattering data to determine the validity of the models.

15. SUBJECT TERMS
Differential cross section; Elastic scattering; Space radiation

16. SECURITY CLASSIFICATION OF:			17. LIMITATION OF ABSTRACT	18. NUMBER OF PAGES	19a. NAME OF RESPONSIBLE PERSON
a. REPORT	b. ABSTRACT	c. THIS PAGE			STI Help Desk (email: help@sti.nasa.gov)
					19b. TELEPHONE NUMBER *(Include area code)*
U	U	U	UU	98	(443) 757-5802